Chemical Engineering Journal 445 (2022) 136605

Contents lists available at ScienceDirect

Chemical Engineering Journal

journal homepage: www.elsevier.com/locate/cej

A global kinetic model for the oxidative dehydrogenation of ethane over mixed metal oxide catalysts at supra-ambient pressures

Jiakang Chen, Zhe Sun, Vemuri Balakotaiah *, Praveen Bollini *

William A. Brookshire Department of Chemical & Biomolecular Engineering, University of Houston, Houston, TX 77204, USA

ARTICLE INFO

Keywords:
M1 phase
Integral kinetics
Mathematical modeling
Autothermal reactors
Global kinetic model

ABSTRACT

Oxidative dehydrogenation of ethane (ODHE), unlike traditional steam cracking processes, can potentially be used to produce ethene at supra-ambient pressures, thereby reducing reactor footprint and alleviating (de) compression energy requirements. Global kinetic models that capture kinetic features of *both* desired and undesired reactions over an extended range of reactant and product pressures are lacking despite the clear reliance of comparative reactor design assessments on such models. We report herein a global kinetic model that accounts for the rates (between 603 and 703 K) of all 6 of the prevalent reaction network steps, extends up to 6 bar total pressure, and explains a broad set of differential and integral kinetic features measured over $MoVTeNbO_x$ catalysts. H_2O_2-mediated dissolution procedures enable low-temperature measurements which under the extended pressure ranges used in this study evidence significant coverages of reduced sites the contributions of which can be interpreted as being determined by ethane to oxygen molar ratios. Explaining measured kinetic features require invoking an oxygen pool present in quasi-equilibrium with gas phase oxygen that is distinct in identity from lattice oxygens, only the latter of which are wholly responsible for hydrogen abstraction steps in turnovers producing ethene, not CO_x. We demonstrate how a simplified global kinetic model that employs power law rate expressions for undesired reactions and excludes product inhibitory effects for the entirety of the reaction network is sufficient to explain both co-feed data as well as differential and integral features evaluated in the absence of product co-feeds. The proposed kinetic model can be employed in comparative assessments of high-pressure ODHE reactor configurations operating non-isothermally, especially those carrying a high sensitivity to contributions from highly exothermic total oxidation reactions.

1. Introduction

Ethene - a key platform molecule used as an intermediate in the production of a variety of bulk chemicals [1] - is currently produced using steam cracking processes that are highly capital, energy, and carbon-intensive [2,3]. Oxidative dehydrogenation of ethane (ODHE) - the O_2-mediated oxidation of ethane to ethene and water at temperatures lower than those corresponding to the steam cracking of ethane - has been extensively evaluated as a less energy-intensive alternative to incumbent processes [4,5]. Of the various classes of catalysts investigated, MoVTeNb-based mixed metal oxide catalysts have exhibited the most promising performance [6–11]; these oxides, comprised of M1, M2, and other unary or binary oxide phases [12–14], oxidize ethane to ethene at remarkably high rates and selectivities, and could potentially enable the implementation of ODHE at temperatures below 673 K [15–18]. A significant body of work on this class of catalysts exists, including prior investigations that have attempted to attribute ethene and oxygenate formation, respectively, to M1 and M2 phases [19–21], to evidence (using experiment and theory) the key role of M1 phase micropores in achieving high rates and selectivities [22,23], and to develop synthetic protocols for improving rates and selectivities by maximizing the abundance of the M1 phase relative to other less desirable ones [24–26]. Despite extensive research, kinetic models that incorporate elements critical to reactor design and scale-up - high reactant conversions and pressures as well as the prevalence of side reactions for example - are for the most part lacking in the literature.

Kinetic models for ethene formation have been reported by the Iglesia group for supported vanadia catalysts [27], by the Lemonidou group for bulk nickel oxide catalysts [28,29], and by the Schmidt group for Pt-coated monoliths [30,31]. Specifically, in the case of $MoVTeNbO_x$ catalysts, Castillo-Araiza and Valente's group [32,33] compared Langmuir-Hinshelwood-Hougen-Watson (LHHW), Mars-van Krevelen (MvK), single site Eley-Rideal, two-site LHHW, and hybrid MvK-LHHW

* Corresponding authors.
E-mail addresses: bala@uh.edu (V. Balakotaiah), ppbollini@uh.edu (P. Bollini).

https://doi.org/10.1016/j.cej.2022.136605
Received 1 March 2022; Received in revised form 21 April 2022; Accepted 23 April 2022
Available online 27 April 2022

Nomenclature

Roman letters

A	heat transfer area,m^2
$C_{p,j}$	specific molar heat capacity of species j,$J/mol/K$
$C_{pv}(T)$	specific volumetric heat capacity of the reaction mixture,$J/(m^3*K)$
D_t	tube diameter,mm
E_a	activation energy, kJ/mol
F_{A0}	molar flow rate at inlet,mol/s
$F_{A,exit}$	molar flow rate at outlet,mol/s
F_j	molar flow rate of species j,mol/s
ΔH_{Rx}	reaction enthalpy,kJ/mol
k_{eff}	effective catalyst thermal conductivity,$W/(m*K)$
k_i	rate constant of step i,$mol/(s*gcat*kPa)$
K_i	equilibrium constant of step i,$mol/(s*gcat*kPa)$
r_j	observed reaction rate,$mol/(s*m^3)$
R	gas constant,$J/mol/K$
S_i	selectivity of product i
T	reaction temperature,K
T_c	coolant temperature,K
T_f	feed temperature,K
ΔT_{ad}	adiabatic temperature rise,K
U	heat transfer coefficient between reactor inside and reactor outside,$W/(m^2*K)$
V	reactor volume,m^3
w_j	weighting factor of species j
ΔW	catalyst weight, g
X_i	conversion of reactant i
$\hat{y}_{i,j}$	kinetic model prediction
$Y_{i,j}$	measured rate under a given set of conditions
z	dimensionless position along the reactor bed

Greek letters:

β_k	estimated parameter k
τ_h	characteristic heat removal time,s
τ_g	characteristic heat generation time,s

models for the ODHE reaction network, and concluded that the single and two-site LHHW models provided the best description of collected data. Although product inhibition terms were used heavily in these studies to obtain reasonable fits with measured rates, their prevalence was not (directly) tested experimentally. Moreover, the vast majority of these previously reported studies focus exclusively on investigating the kinetics of ethene formation over $MoVTeNbO_x$ catalysts, and not those of undesired reactions, due in part to the exceptionally high ethene selectivities (>90%) achieved despite high ethane conversions (60%) over a wide range of temperatures [34,35]. The significantly more exothermic nature of primary and secondary deep oxidation reactions, however, can potentially result in a disproportionately large impact of their rate parameters on the feasibility of specific reactor design configurations, especially those operating closer to adiabatic conditions. Additionally, rates of these highly exothermic undesired reactions over $MoVTeNbO_x$ catalysts have been reported to exhibit greater sensitivities to temperature, as reflected by the larger magnitude of their corresponding apparent activation energy values compared to ethene formation [36,37]; these larger apparent activation energies and heats of reaction render their rate parameters to be critical elements within reactor modeling efforts aimed at maximizing ethene productivity by achieving optimal control over spatiotemporal temperature profiles. In our prior work, we employed kinetic models that exclude side reactions to suggest that autothermal reactor configurations compare favorably with cooled multitubular ones, with the achievement of requisite heat removal rates for the latter configuration appearing to be predicated on the application of sufficient levels of catalyst dilution [38]. We surmise that the inclusion of kinetic and thermodynamic features corresponding to side reactions should amplify the favorability of autothermal configurations relative to cooled multitubular ones, yet have no means of evidencing such a premise owing to the dearth of ODHE models that capture global kinetic features.

The operation of steam cracking processes are limited not only to high temperatures but also to low pressures (with steam as diluent) to maximize ethane conversion and minimize coke disposition rates [39]; these low operating pressures result in high compression costs that account for up to 15% of total energy consumed in steam cracking processes that also co-produce hydrogen [40]. Exothermic ODHE processes, on the other hand, are not constrained to operation at low pressures, and hence create opportunities for the intensified production of ethene in compact reactors amenable to modular operation. Despite oxidative routes enabling high-pressure ethene production, few publications report the effect of pressure on ODHE kinetics over $MoVTeNbO_x$ catalysts [41], and even the ones that do, do so merely to report phenomenological relationships between operating pressure and catalyst performance/stability. In this work, we report a global kinetic model for ethane oxidation over $MoVTeNbO_x$ catalysts. The model explains the dependence of rates and product distributions as a function of residence time, the effect of co-feeds on product formation rates, and differential and integral rate data obtained over a wide range of temperatures and operating pressures (603–703 K, 1–6 bar total pressure). Operation over an extended pressure range provides access to non-negligible coverages of reduced sites as a consequence of the larger ethane to oxygen molar ratios explored, and the inclusion of side reactions in the kinetic model suggest the involvement of multiple oxygen species - some in quasi-equilibrium with gas phase oxygen and others that are not - in ethane oxidation over $MoVTeNbO_x$ catalysts. The model provides a tool for addressing critical unanswered questions in the ODHE literature, including the comparative assessment of reactor designs for high pressure operation, as well as the role of highly exothermic total oxidation steps in altering the relative feasibility of various reactor designs, especially those more proximal to adiabatic operation.

2. Experimental section

2.1. Catalyst synthesis

Detailed synthesis procedures for the $MoVTeNbO_x$ mixed metal oxide catalysts used in our study have been reported as part of a previous publication [38], the main steps of which can be summarized as follows: ammonium molybdate tetrahydrate (Sigma Aldrich, ≥ 99.0%), vanadyl sulfate (Sigma Aldrich, ≥ 97.0%), telluric acid (Sigma Aldrich, ≥ 98.0%) and ammonium niobate oxalate hydrate (Sigma Aldrich, ≥ 99.99%) were dissolved into 75 ml deionized water to form a dark violet solution with a Mo:V:Te:Nb molar ratio of 1:0.25:0.17:0.12. The solution was autoclaved at 448 K for 48 h and subsequently washed with 1 L of deionized water, centrifuged, and dried overnight at 353 K. The precipitate obtained after drying the sample overnight was calcined at 873 K for 2 h under inert flow. Dissolution of part of the catalyst - presumably the M2 phase - was achieved by washing the calcined powder obtained above in a 30% hydrogen peroxide solution (Macron Fine Chemicals) at room temperature for 24 h (0.05g solid per ml solution). The resulting suspension was washed with a liter of deionized water, vacuum filtered, and dried overnight at 353 K. The dried solid was then re-calcined using

the same procedure as described above for the sample prior to H_2O_2 treatment.

2.2. Sample characterization

Synthesized catalyst samples were characterized using X-ray diffraction (XRD), N_2 physisorption, scanning electron microscopy (SEM), and inductively coupled plasma (ICP) analysis. Powder XRD patterns were obtained using a Panalytical diffractometer (Empyrean Series 3) with CuKα radiation ($\lambda = 0.154$ nm, tube voltage: 45 kV, tube current: 40 mA) over a 5-50° angular range using a 0.0001° step size with a scan rate of 0.06°/s. N_2 physisorption measurements were conducted at 77 K on a Micromeritics 3FLEX instrument after degassing the sample for 3 h under vacuum ($P \approx 1 \times 10^{-4}$) at 573 K, and the data treated according to the Brunauer-Emmett-Teller (BET) adsorption isotherm equation in the$p/p_0 = 0.05$–0.30 pressure range. Sample morphology was assessed using images obtained on a LEO 1525 FEG scanning electron microscope with an accelerating voltage of 3 KV. Catalyst composition was determined using an AGILENT 725 ICP-OES system, with the sample being dissolved into a mixture of HF and HNO_3. Detailed characterization results are presented in sections S2-S5 of the Supporting Information.

2.3. Reactor setup

Kinetic data were obtained in a stainless-steel fixed bed reactor with an inner diameter of 4 mm (Figure S1, SI). The temperature was measured using two K-type thermocouples, one placed horizontally along the center of the furnace in proximity to the heating element, and the other touching the outer surface of the stainless-steel tube at the midpoint of the bed in the axial direction. Two Swagelok K-series back pressure regulators were installed at the ends of the reactant and bypass lines to maintain high pressure. The M1 phase catalyst was crushed using a mortar and pestle and pelletized under a pressure of 2500 psi to a 40–80 mesh size range and used without any dilution. Most of the kinetic tests were performed over a bed of 0.1 g catalyst with a length of 4.5 mm. Pre and post-catalytic sections were filled with untreated silicon beads of 20 mesh size (Thermo Scientific) to hold the catalyst bed in place and reduce axial temperature gradients [42]. Flow rates of all gases (C_2H_6, O_2, C_2H_4, CO, CO_2, He, CH_4) were controlled using mass flow controllers (Brooks instruments), with helium and methane (Matheson > 99.999%) used as diluent and internal standard, respectively. Water vapor was co-fed into the reactor system using a syringe pump (KDS 100 Legacy) attached to a liquid injection port, and all transfer lines were heated to temperatures in excess of 433 K to prevent condensation of water at elevated pressures. The catalyst was heated to reaction temperature under helium before switching the bed inlet to the desired feed composition. Quantitative analysis of inlet and outlet stream compositions were conducted using an online gas chromatograph (Agilent 7890B) equipped with an Agilent Gas Pro column (inner diameter: 0.32 mm, length: 60 m) and flame ionization and thermal conductivity detectors downstream of the column. Blank tube tests without any catalyst loaded that were conducted at 773 K (i.e. 70 K above the temperature range of our experiments) and a contact time of 0.5 s resulted in ethane and oxygen conversions less than 1%. Kinetic data over a wide range of temperatures, contact times, and pressures were used to develop the model presented in this work (Table 1); reaction temperatures were varied from 603 to 703 K, contact times were varied between 0.04 and 1.5 s, and inlet partial pressures of C_2H_6, O_2, C_2H_4, CO, and CO_2 spanned 5–500 kPa, 5–500 kPa, 5–100 kPa, 5–30 kPa, and 2–10 kPa, respectively. Ethane and oxygen conversions were kept below 5% in differential measurements that constitute the vast majority of the experiments reported here. C_2D_6 (Cambridge Isotope Laboratories, > 98%) was used without further purification in isotopic experiments conducted to probe the kinetic relevance of C–H scission steps. All of the reported experimental data are steady-state values obtained as an average of three to four data points. Criteria used to exclude concentration and temperature gradients are discussed in detail in section S6 of the Supporting Information. Values of catalyst bulk density, catalyst particle density and pore volume, and effective thermal conductivity used in these calculations are 1600 kg/m^3, 2400 kg/m^3, 0.0224 cm^3/g and 0.15 W/(m·K), respectively. Criteria for eliminating transport-related artifacts were found to be satisfied even under the most severe conditions (low flow rates, high temperatures), justifying the use of a 1D pseudo-homogeneous model to describe integral data. Carbon balances were>95% for all data reported (Section S1, SI). The conversion of ethane and oxygen, as well as their carbon selectivity were defined as below:

$$X_i = \frac{F_{i,\,Inlet} - F_{i,\,outlet}}{F_{i,\,Inlet}} \text{for i} = C_2H_6,\ C_2H_4,\ and\ O_2 \tag{1}$$

$$S_i = \frac{2F_i}{2F_{C_2H_4} + F_{CO} + F_{CO_2}} \text{ for i } = C_2H_4 \tag{2}$$

$$S_j = \frac{F_j}{2F_{C_2H_4} + F_{CO} + F_{CO_2}} \text{for j} = CO\ and\ CO_2 \tag{3}$$

where X_i represents the conversion of the reactant, S_i/S_j are product selectivities, and F_i represents reactant/product molar flow rates.

3. Reactor model and kinetic parameter estimation

Differential measurements were conducted at low reactant conversions (less than 20%) in the absence of significant product inhibitory effects (section 4.2). Reported reaction rates under differential conditions were calculated as:

$$-r_A = \frac{F_{A0} - F_{A,exit}}{\Delta W} \tag{4}$$

A 1D pseudo-homogeneous plug flow reactor model was used to treat high conversion (integral) data using the following mole balance:

$$\frac{dF_j}{dz} = Vr_j, \quad \text{j} = 1, 2, \cdots, \text{m};\ F_j = F_{j0} \text{ at z} = 0 \tag{5}$$

The following equation was used to describe the energy balance:

$$\frac{dT}{dz} = \frac{Vr(-\Delta H_{Rx}) - AU(T - T_c)}{\sum_{j=1}^{m} F_j C_{p,j}}, \quad \text{j} = 1, 2, .., \text{m};$$
$$\text{T} = \text{T}_0 \text{ at } z = 0 \tag{6}$$

Kinetic parameters were estimated by minimizing a weighted objective function:

Table 1
Reaction conditions used to construct the global kinetic model.

T (K)	$P_{C_2H_6}$(kPa)	P_{O_2}(kPa)	$P_{C_2H_4}$(kPa)	P_{CO}(kPa)	P_{CO_2}(kPa)	P_{H_2O}(kPa)	P_{total}(bar)
603–703	5–480	5–480	5–100	2–30	2–10	5–10	1–6
$X_{C_2H_6}$(%)	X_{O_2} (%)	$X_{C_2H_4}$(%)	$S_{C_2H_4}$ (%)	S_{CO}(%)	S_{CO_2} (%)	τ (s)	
1.57–70.69	0.32–88.04	0.24–6.48	89.54–97.50	0.76–4.70	1.52–4.33	0.04–1.5	

$$RSS\left(\beta_{-}\right)=\sum_{i=1}^{n_{exp}}\sum_{j=1}^{n_{resp}} w_j\left(Y_{i,j}-\hat{y}_{i,j}\right)^2 \xrightarrow{\beta_1,\beta_2\cdots\beta_k\cdots\beta_{n_p}} min, \quad (7)$$

where $Y_{i,j}$ represents experimentally measured rates under specific sets of conditions, $\hat{y}_{i,j}$ represents kinetic model predictions, n_{exp} represents the number of experiments used in the parameter estimation process, n_{resp} the number of responses for each experiment, β_k the estimated parameters, and w_j the weighting factors used for assigning relative importance to specific experiments used in the parameter estimation procedure. For example, weighting factors for CO_x formation rates are typically 10 times higher than those for ethane and ethene formation.

Parameter estimation was conducted in three steps: first, kinetic parameters corresponding to ethane partial oxidation to ethene were estimated from data collected under experimental conditions where ethene carbon selectivities exceeded 95%. Second, kinetics of a sub-network containing secondary reactions (steps 4–6) were analyzed by feeding ethene and oxygen (in the absence of ethane) directly over the catalyst bed. In the third and final step, kinetics of the entire 6-step reaction network were analyzed, with parameters determined from the previous two steps being used as initial guesses in the regression procedure.

4. Results and discussion

4.1. Identification of CO_x formation routes

Ethane oxidation over bulk metal oxide catalysts proceeds through primary and secondary reaction steps depicted in Scheme 1. The desired product – ethene – is produced through the primary partial oxidation of ethane (step 1, Scheme 1) and consumed in secondary reactions producing total oxidation products CO (step 4) and CO_2 (step 5). Total oxidation products – CO and CO_2 – do not necessarily originate from secondary reactions involving ethene, but instead can be formed through the direct oxidation of ethane in primary reaction steps comprising a single catalytic sojourn on the oxide surface (steps 2 and 3). Oxidation of CO to CO_2 closes out the 6-step reaction network under consideration in this study focused on modeling experimental conditions under which C_2 oxygenates are produced below detection limits, unlike some previous studies that report acetic acid and acetaldehyde formation at elevated pressures (1–2 MPa) and low temperatures (473–573 K) [43]. The greater proportion of the M1 phase in our H_2O_2-treated samples also serve to minimize formation of C2 oxygenates. Minute amounts of such C2 oxygenates (acetic acid + acetaldehyde) that may be formed in our experiments but remain below detection limits can be considered to be lumped into CO_2 formation rates without major implications on the conclusions of the study. Ethene selectivities between 603 and 703 K remain above 89% even at ethane and oxygen conversions as high as 60%, rendering quantification of CO and CO_2 highly challenging.

Identifying reactions within the overall network that require consideration constitutes the first step in the development of a global kinetic model. Oyama et al. proposed a 9-step ODHE reaction network over a V_2O_5/SiO_2 catalyst where ethene and acetaldehyde were the desired products measured [44]. Donaubauer et al. developed a 5-step reaction scheme over a $MoVTeNbO_x$ catalyst, and claimed that ethane oxidation produces acetic acid in addition to ethene, with CO_2 being formed exclusively through decomposition of the former, not the latter [45]. Quintana-Solórzano et al. included in their analysis all primary and secondary reaction steps except for the oxidation of CO [33], the prevalence of which under reaction conditions used in our study is demonstrated using CO co-feed experiments discussed in section 4.2.

We use selectivity-conversion plots to understand the prevalence of primary and secondary routes for CO_x formation, and to assess whether the contributions of any of the steps in Scheme 1 are negligible under the conditions used in our study; specifically, finite molar selectivities at zero residence time are indicative of primary routes for product formation [46,47]. Selectivity trends extrapolated to zero conversion point to ethene as the major product formed in primary reactions (Figure 1a, 643 K, 12 kPa C_2H_6, 6 kPa O_2); non-zero selectivities of both CO and CO_2 when extrapolated to zero conversion indicate their formation through the direct oxidation of ethane in primary steps. Ethene selectivities decrease, and CO and CO_2 selectivities increase with increasing ethane conversion, consistent with the formation of total oxidation products not just through primary steps but also additionally through non-primary reactions involving the oxidation of ethene to either CO or CO_2, the contributions of which increase with increasing ethane conversion. Unlike ethene oxidation (step 4, Scheme 1), which represents the only non-primary route for CO formation, CO_2 can be formed either through secondary reactions involving the oxidation of ethene to CO_2 (step 5) or the oxidation of CO that is formed through ethene oxidation (step 4 followed by step 6). Selectivity-conversion plots for ethene oxidation provide suggestions as to the identity of non-primary pathways for CO_2 formation (Figure 1b, 663 K, 25 kPa C_2H_4, 25 kPa O_2); non-zero initial CO_2 selectivities in experiments evaluating the oxidation of ethene suggest that part of its formation is attributable to turnovers involving the direct oxidation of ethene to CO_2. Selectivity to CO_2 increases with ethene conversion at the expense of that of CO (Fig. 1b), consistent with increasing contributions of CO oxidation toward CO_2 formation with increasing ethene conversion. Such finite CO_2 selectivities that increase with ethene conversion suggest that both direct (step 5) and indirect (step 4 followed by step 6) routes contribute to CO_2 formation during ethane oxidation over the $MoVTeNbO_x$ catalyst formulation used in our study; considering only parallel routes for ethane/ethene oxidation to CO and CO_2 (steps 2 and 3 or steps 4 and 5, respectively) may not be

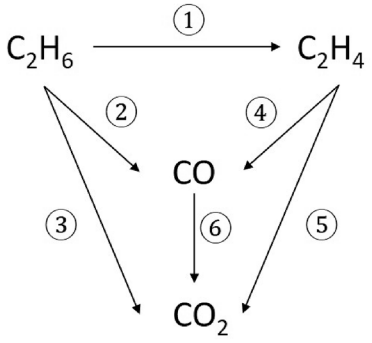

Step 1: $C_2H_6 + 0.5O_2 \rightarrow C_2H_4 + H_2O$

Step 2: $C_2H_6 + 2.5O_2 \rightarrow 2CO + 3H_2O$

Step 3: $C_2H_6 + 3.5O_2 \rightarrow 2CO_2 + 3H_2O$

Step 4: $C_2H_4 + 2O_2 \rightarrow 2CO + 2H_2O$

Step 5: $C_2H_4 + 3O_2 \rightarrow 2CO_2 + 2H_2O$

Step 6: $CO + 0.5O_2 \rightarrow CO_2$

Scheme 1. Schematic of possible reaction steps involved in ethane oxidation over $MoVTeNbO_x$ catalysts: 1) primary oxidation of ethane to ethene 2) primary oxidation of ethane to CO 3) primary oxidation of ethane to CO_2 4) secondary oxidation of ethene to CO 5) secondary oxidation of ethene to CO_2 and 6) secondary oxidation of CO to CO_2.

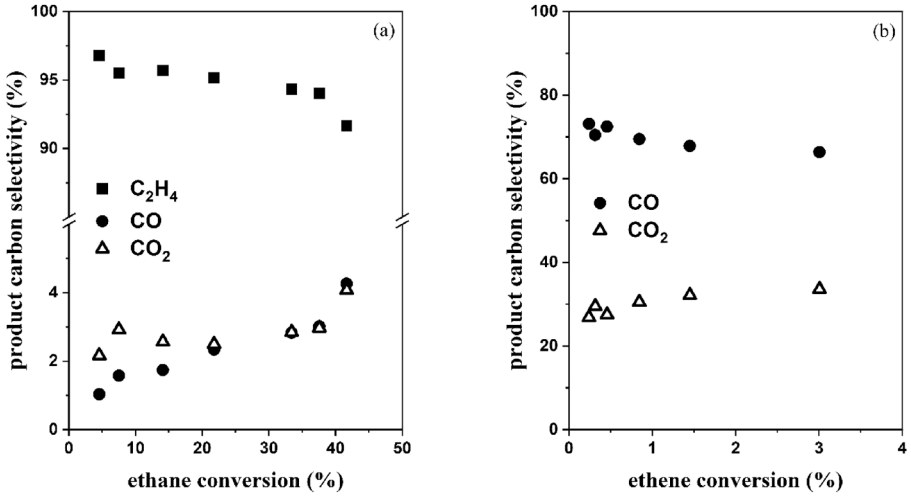

Fig. 1. Product carbon selectivity as a function of (a) ethane conversion; reaction conditions: 643 K, 12 kPa C_2H_6, 6 kPa O_2, balance He at 1 bar, contact time: 0.04–0.66 s (b) ethene conversion; reaction conditions: 663 K, 25 kPa C_2H_4, 25 kPa O_2, balance He at 1 bar, contact time: 0.01–0.11 s.

sufficient to accurately capture kinetic phenomena pertaining to the formation of undesired total oxidation products. Overall, the selectivity-conversion data in Fig. 1 suggest that the rates of *all* 6 steps in the ODHE reaction network may need to be considered to accurately describe reactor temperature gradients, steps the rate of which are especially important to capture given the significantly more exothermic nature of CO_2 formation routes compared to CO formation routes. We emphasize herein the fact that contributions of CO oxidation toward CO_2 formation are non-negligible even at ethene conversions as low as 3%; note that these ethene conversions at 663 K result in CO:ethene molar ratios (~0.018, Fig. 1b) that can still be exceeded by those encountered at 40% ethane conversion at 643 K (~0.09, Fig. 1a) despite the highly selective nature of the catalyst under consideration. CO oxidation rates therefore have to necessarily be included in our global kinetic model, and accounting for them assumes greater importance with increasing ethane conversion. We next assess contributions of product inhibition effects that have commonly been used in prior studies to add fitting parameters that (somewhat inevitably) improve agreement between model predictions and regressed rate data.

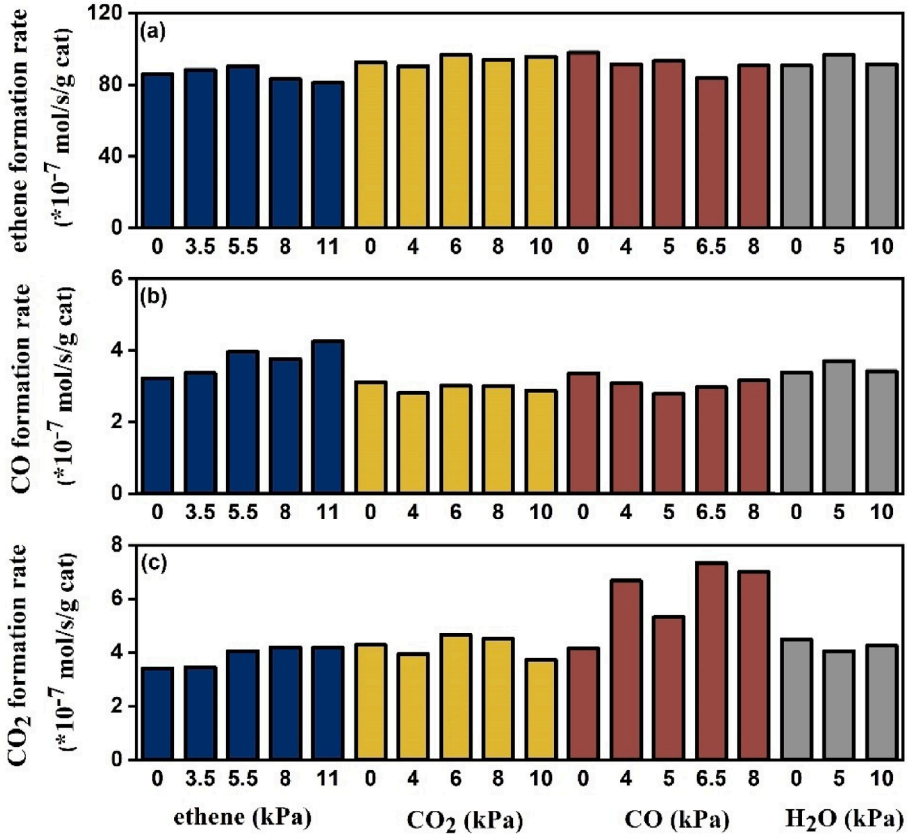

Fig. 2. Product formation rates for (a) ethene (b) CO and (c) CO_2 over 0.1 g MoVTeNbOx catalyst at 663 K in the presence of ethene, CO, CO_2 and water co-feeds with the baseline non co-feed gas mixture corresponding to 50 kPa C_2H_6, 25 kPa O_2, and balance He at 6 bar total pressure, 120 sccm total flow at atmospheric pressure.

4.2. Assessment of product inhibition

Product inhibition - especially water inhibition resulting from the reversible nature of recombinative water desorption steps - are commonly encountered in catalytic partial oxidation reactions over bulk metal oxides [48–50]. More specifically, ethane partial oxidation rates have been shown to be sensitive to water pressure over supported vanadia [51] and molybdenum oxides [51,52], as well as bulk nickel oxide [53]. Oxidation rates on bulk metal oxides can also be inhibited by CO_2, as is the case over nickel oxide catalysts that tend to form non-stoichiometric oxygen derived carbonate species the equilibrium coverages of which increase monotonically with CO_2 pressure [54,55], and as evidenced by the carbonate-mediated inhibition of methane oxidation rates over rare earth oxide catalysts [56–58]. Although the prevalence of water inhibition over $MoVTeNbO_x$ catalysts has been evaluated in the literature, the sensitivity of rates of undesired reactions to water and CO_2 pressures has thus far not been tested – sensitivities important to capture in the global kinetic model being developed in this study.

The (in)significance of product inhibition effects on rates of both desired and undesired reactions were evaluated using product co-feed experiments. Ethene formation rates were found to be independent of CO_2 (0–10 kPa), CO (0–8 kPa), and water (0–10 kPa) co-feed partial pressures (Fig. 2a), suggesting a lack of carbonate formation under reaction conditions, and consistent with the involvement of recombinative water desorption steps that are irreversible in nature (further discussion in section 4.3). Ethene formation rates, therefore, can be expressed as a function of ethane and oxygen partial pressures without the inclusion of functional dependencies on the partial pressures of products of any of the reactions in the reaction network under consideration. CO formation rates were also found to be insensitive to product partial pressures but dependent on ethene partial pressure; formation rates increase roughly 25 % (3.36×10^{-7} to 4.25×10^{-7} mol s^{-1} g_{cat}^{-1}) as ethene partial pressures increase from 0 to 11 kPa (Fig. 2b), suggesting that CO formation rates from ethene and ethane (present at 50 kPa) may be comparable under certain conditions and that the significantly stronger C–H and C–C bonds in ethene compared to ethane do not necessarily result in negligible relative contributions of ethene oxidation toward CO formation (C–H bond dissociation energies: 476 and 435 kJ/mol [59] and C–C bond dissociation energies: 720.5 [60] and 377.4 kJ/mol [61] for ethene and ethane, respectively). Similar co-feed experiments were performed to probe the dependency of CO_2 formation rates on ethene, CO, CO_2 and water partial pressures (Fig. 2c). CO_2 formation rates exhibit a dependency not only on ethene pressure but also on CO co-feed pressure (4.1×10^{-7} to 7.0×10^{-7} mol s^{-1} g_{cat}^{-1} as P_{CO2} increases from 0 to 8 kPa), indicating plausible contributions of CO oxidation toward CO_2 formation under ODHE conditions, and reinforcing contributions from the same that are reflected in significant increases in CO_2 selectivity with residence time during ethene oxidation at ethene conversions as low as 3% (Fig. 1b).

Product inhibition effects in secondary reactions were probed explicitly in ethene oxidation experiments where the effect of ethane, CO, and CO_2 co-feeds on product formation rates were measured. CO formation rates increase with ethane co-feed pressure, but remain insensitive to CO_2 co-feed pressure (Figure S5(a), SI), further corroborating the lack of product inhibition in CO oxidation steps. CO_2 formation rates increase with ethane and CO co-feed pressures, consistent with the prevalence of direct (step 3) and series (step 2 followed by step 6) pathways for producing CO_2. The lack of product inhibition simplifies significantly the functional forms of rate expressions required to capture differential and integral kinetic features presented, and also render unnecessary the calculation of initial rates through extrapolations to zero conversion/residence time that the rigorous development of global kinetic models would otherwise be predicated on. We next use partial pressure dependencies of the rates of these various reactions to develop individual rate expressions that constitute a global kinetic model that explain high-pressure ODHE kinetic data over a relatively large range of reaction temperatures (603 K −703 K).

4.3. Kinetic model rate expressions

4.3.1. Ethane oxidation kinetics

We propose herein a plausible sequence of steps mediating primary ethane partial oxidation to ethene and total oxidation to CO_x that are consistent with experimentally measured partial pressure dependencies and kinetic isotope effects. Partial oxidation rates (step 1, Scheme 1) are readily accessible in our experiments, especially at low ethane conversions, owing to the exceptionally high ethene selectivities (>95%) exhibited by the $MoVTeNbO_x$ catalysts employed in our study. ODHE rates at 603 K were found to exhibit fractional order dependency in both ethane and oxygen (Fig. 3a and b), unlike our previous study that reported first order and zero order behavior in ethane and oxygen, respectively [38], due in part to the higher temperatures (703 K) and smaller range of pressures (6–30 kPa ethane and 6 kPa O_2) explored in that study, and also possibly even due to differences in catalyst surface properties originating from H_2O_2-mediated dissolution procedures employed herein. More specifically, partial oxidation rates appear to be first order in ethane at sufficiently low pressures of ethane regardless of oxygen pressure, and transition to fractional order dependency at higher ethane pressures (Fig. 3a). The decrease in sensitivity to ethane pressure and the approach to zero order behavior occurs at progressively lower ethane pressures with a decrease in oxygen pressure (50–25-10 kPa O_2, Fig. 3a). Rates also transition from being first order in oxygen at low oxygen pressures to being insensitive to the same at higher oxygen pressures, with first order behavior being achieved at progressively lower oxygen pressures with decreasing ethane pressure (50–25-10 kPa ethane, Fig. 3b). These kinetic features can be rationalized neither on basis of trends in reactor non-isothermality as reflected by conversion-scaled adiabatic temperature rise values as a function of reaction conditions (Section S18, SI), nor using quasi-equilibrated dissociative oxygen adsorption steps postulated in our previous study on non-H_2O_2 treated $MoVTeNbO_x$ samples that tie reduced site coverages (and concomitant oxygen pressure dependencies) exclusively to oxygen, not ethane pressures [38]. Relative coverages of reduced sites are instead postulated to be governed by ethane to oxygen molar ratios, as would be necessitated by a balance (at steady state) between the rates of consumption and production of lattice oxygen in irreversible hydrogen abstraction and dissociative oxygen adsorption steps, respectively (*vide infra*).

The second kinetic feature identified in the data reported here relates to the significantly greater oxygen sensitivities of ethane total oxidation rates compared to ethane partial oxidation rates at 643 K, with these higher temperatures being necessary for the accurate measurement of total oxidation rates that tend to remain an order of magnitude or two lower than partial oxidation rates (Figure S6, SI). Accurate measurements of total oxidation rates were rendered especially challenging due to the fact that ethane conversions had to be maintained below 5.8% to minimize contributions from secondary ethene and CO oxidation reactions that become prevalent at high conversions. Ethane total oxidation rates at 643 K are almost linear in ethane pressure and close to half order in oxygen pressure (Fig. 4), in contrast with partial oxidation rates under identical conditions that are first order in ethane and zero order in oxygen (Figure S6A, SI). Michaels et al. [62,63] have previously noted zero order and half order rate behavior in oxygen for partial and total oxidation, respectively, over a Mg-V-Sb ternary oxide catalyst. Similarly, Gaab et al. reported CO_2 formation rates that are half order in oxygen and CO formation rates that are 0.27 order in oxygen over an Li/Dy/Mg/O/(Cl) mixed metal oxide catalyst [64]. Plausible mechanisms for ethane oxidation must not only explain the aforementioned ethane and oxygen partial pressure dependencies of ethene formation rates but also the significantly greater oxygen sensitivities of ethane total oxidation rates compared to ethane partial oxidation rates.

Four classes of Mars-van Krevelen reaction schemes (depicted in

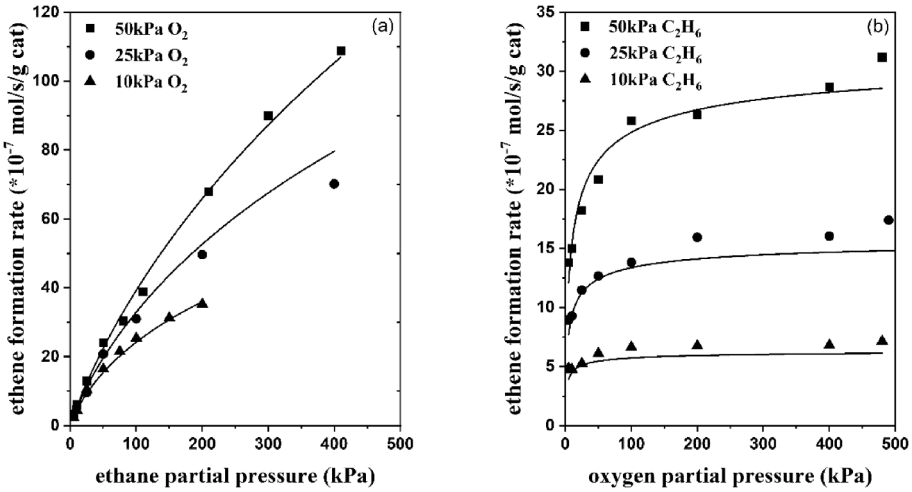

Fig. 3. Effects of (a) ethane and (b) oxygen partial pressure on ethene formation rate over 0.1 g $MoVTeNbO_x$ at 603 K with He as inert carrier at 6 bar total pressure, 120 sccm total flow at atmospheric pressure. Solid lines represent model predictions and symbols represent experimental data.

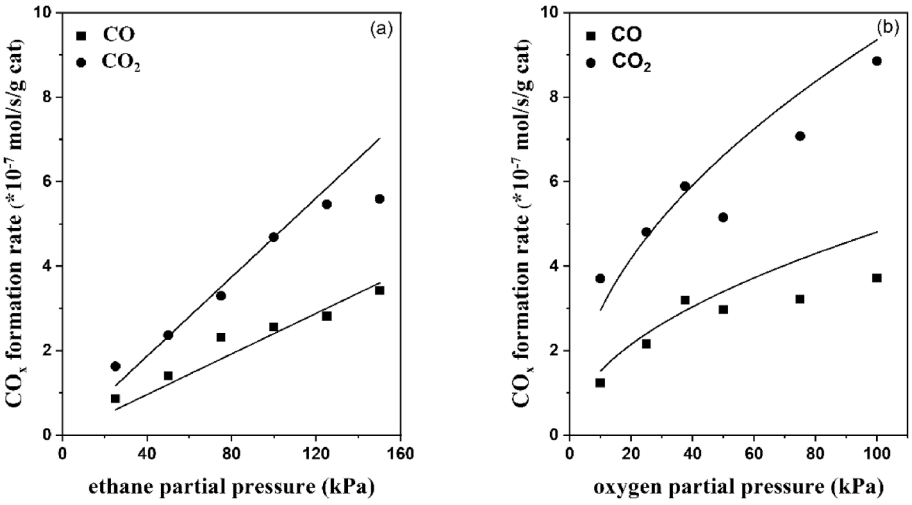

Fig. 4. Ethane total oxidation rates as a function of (a) ethane partial pressure at 25 kPa O_2 and (b) oxygen partial pressure at 100 kPa C_2H_6 over 0.1 g $MoVTeNbO_x$ at 643 K with He as inert carrier at 6 bar total pressure; ethane conversions were maintained below 5.8%. Solid lines represent model predictions and symbols represent experimental data.

Scheme 2) were evaluated in the context of interpreting the aforementioned observations and kinetic isotope effects discussed later in this section. The first mechanistic scheme evaluated involves a single type of lattice oxygen species formed in irreversible O_2 dissociative adsorption steps (Scheme 2a). Ethane physisorbs onto lattice oxygen in a quasi-equilibrated step, followed by hydrogen abstraction by a neighboring lattice oxygen. ß-hydride elimination to form ethene is then followed by irreversible recombinative water desorption steps that form oxygen vacancies subsequently refilled by O_2 dissociative adsorption. The decomposition of the ethoxide intermediate represents a branching point in this mechanism, with ß-hydride elimination resulting in desired turnovers producing ethene, and the involvement of an oxygen atom adjacent to the ethoxide intermediate resulting in CO_x formation. The precise nature of bond scission and bond forming events remain inaccessible to us given the limitations of the experimental toolkit employed in this work, and could constitute the focus of future studies. Assuming ethane adsorption to be quasi-equilibrated, and applying the pseudo steady state assumption to ethoxide, hydroxyl, and lattice oxygen species leads to the following expression for the ratio of rates of ethene and CO_x formation (derivation in section S8, SI):

$$\frac{r_{C_2H_4}}{r_{CO_x}} = \frac{\frac{k_3}{2k_4}}{1 + K_1[C_2H_6] + \sqrt{\frac{k_2K_1[C_2H_6]}{k_5}} + \sqrt{\frac{k_2k_4K_1[C_2H_6]}{2k_3k_6[O_2]}}} \quad (8)$$

where the meaning of kinetic and thermodynamic parameters in this equation are described in section S8 of the Supporting Information. Ethene to CO_x rate ratios that are near-invariant in ethane pressure and negative half order dependent in oxygen pressure (Figure S6B) cannot be rationalized using rate ratios described using equation (8), suggesting the need for an alternative mechanistic scheme. We emphasize here the fact that Scheme 2a leads to the expected qualitative features in Fig. 3 for ethane partial oxidation, but do not explain accurately the significantly greater sensitivities to oxygen pressures, but not ethane pressures, exhibited by total oxidation rates (Figure S6B).

A second, alternative scheme adapted using mechanistic suggestions put forth by the Deshlahra group [21,65] was also evaluated (Scheme 2b). Physisorbed ethane formed in a quasi-equilibrated step decomposes directly to produce adsorbed ethene in a single step involving a single active site, unlike the ethoxide formation pathway in Scheme 2a that postulates hydrogen abstraction by a neighboring lattice oxygen. Adsorbed ethane represents a branching point in this reaction scheme,

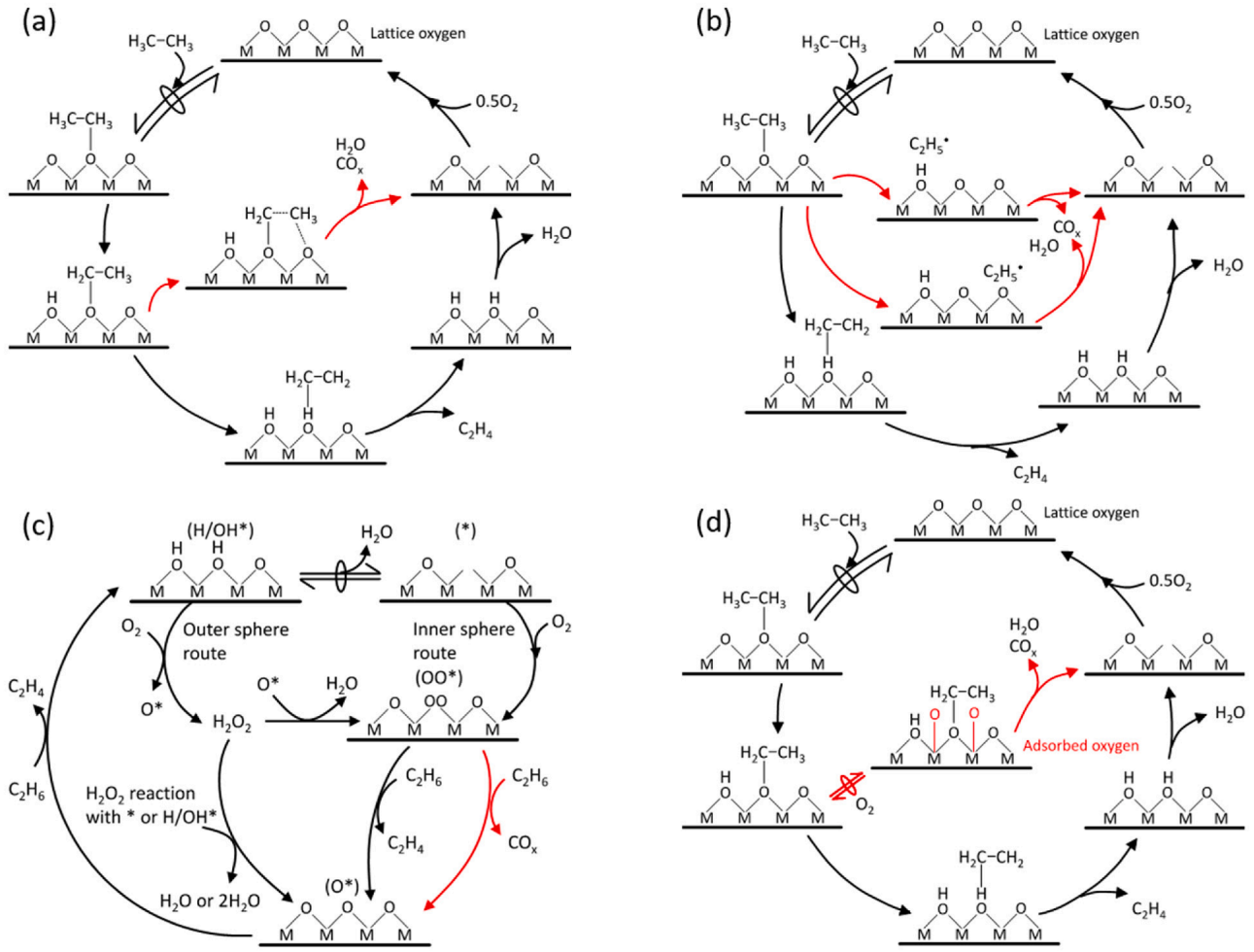

Scheme 2. Classes of Mars-van Krevelen cycles evaluated in interpreting ethane primary oxidation data (a) single oxygen site model with two proximal lattice oxygen sites involved in hydrogen abstraction steps (b) single site model without hydrogen abstraction by a proximal oxygen [21,65] (c) single oxygen site model accounting for inner and outer sphere reoxidation routes [66] (d) dual oxygen site model involving lattice oxygen formed in irreversible dissociative adsorption steps and adsorbed oxygen present in quasi-equilibrium with gas phase dioxygen. Undesired steps leading to CO_x formation are highlighted in red. Oval symbols on arrows are used to represent steps assumed to be quasi-equilibrated.

with hydrogen abstraction resulting in a radical-like intermediate that upon interaction with a neighboring lattice oxygen forms CO_x. This reaction scheme, which postulates the involvement of neighboring lattice oxygens in CO_x formation steps but not ethene formation steps leads to the following ethene to CO_x formation rate ratio when applying the pseudo steady state hypothesis to the C_2H_5, OH/MOH* $-C_2H_4$, M*, and OH/MOH* intermediates (derivation in Section S9, SI):

$$\frac{r_{C_2H_4}}{r_{CO_x}} = \frac{0.5k_2K_1[C_2H_6]}{k_4K_1[C_2H_6] + \frac{k_4k_6K_1 * \frac{(k_2+k_4)K_1[C_2H_6]^2}{k_5}}{k_7 + \frac{k_4k_6K_1[C_2H_6]}{k_5}}} \quad (9)$$

where the meaning of kinetic and thermodynamic parameters in this equation are described in section S9 of the Supporting Information. The strong dependence of ethene to CO_x rate ratios on oxygen pressure cannot be captured using equation (9), suggesting Scheme 2b to be inconsistent with the kinetic data reported in Figures 3, 4, and S12.

The lack of consistency between experimentally measured kinetic features and rate ratios derived for reaction schemes involving a single type of active oxygen species led us to considering the involvement of additional active oxygen species that participate in total oxidative turnovers, but not necessarily in partial oxidative turnovers producing the desired product. The first such scheme considered accounts for inner and outer sphere routes for reoxidation of isolated two-electron reduced centers on sparsely reduced oxide surfaces presumed to be involved in kinetically irrelevant oxidation cycles (Scheme 2c). These routes have previously been analyzed and evidenced experimentally during alkanol oxidation using four-electron oxidants over supported polyoxometalate clusters exhibiting kinetically demanding oxygen diffusion steps [66,67], but not, to the best of our knowledge, been assessed rigorously for alkane oxidation over bulk metal oxides. Notably, active oxygen intermediates formed during O_2 activation on two-electron reduced centers have been invoked heavily in the enzyme catalysis literature [68–70], and also been proposed to be involved in undesired reaction steps during the oxidative dehydrogenation of propane over supported vanadia catalysts [71]. Two possible routes for reoxidation of two-electron reduced centers (H/OH*) to lattice oxygen (O*) exist (Scheme 2c) – outer sphere routes that circumvent scission and formation of metal–oxygen bonds, and inner sphere routes that rely on such scission/formation steps being kinetically accessible. The H/OH* reduced center undergoes recombinative water desorption to produce an oxygen vacancy *, that can then undergo reoxidation through steps constituting inner sphere routes. The adsorption of dioxygen onto a vacancy generates a peroxo intermediate that can be consumed in either ethane partial oxidation to ethene or total oxidation to CO_x, both of which regenerate lattice oxygen species O*. These lattice oxygens can also be regenerated directly from H/OH* reduced centers through outer sphere routes that circumvent metal–oxygen bond scission. Gas phase

dioxygen reacts with these reduced centers as part of outer sphere routes to form H_2O_2. H_2O_2 can further react with another two-electron reduced center (* or H/OH*) to close out the four-electron redox cycle and regenerate lattice oxygen (O*). Lastly, H_2O_2 can allow for an interconversion between the two types of active oxygen - lattice oxygen and peroxo intermediates – thereby increasing the relative contribution of inner sphere routes to reoxidation cycles. This reaction scheme leads to the following expression for ethene and CO_x formation rate ratios (Section S10, SI):

$$\frac{r_{C_2H_4}}{r_{CO_x}} = \frac{(k_3 + k_4)\left(1 + \alpha\frac{k_2[C_2H_6]}{2k_7[O_2]}\right)}{k_4} + \frac{k_3}{2k_4} \quad (10)$$

where the meaning of kinetic and thermodynamic parameters in this equation are described in section S10 of the Supporting Information. Ethene to CO_x rate ratios are predicted to decrease with increasing oxygen pressure, consistent with the rate data reported in section S12, but not necessarily with a negative 0.5 order dependency as suggested by experimentally measured rate data. Eq. (10) also suggests a concurrent positive order dependency on ethane partial pressures, in contradiction with the trends reported in our work. More extended descriptions of the oxidation half cycle such as the ones considered in Scheme 2c, therefore, also appear to not provide an accurate description of primary oxidation rate data despite the postulation of an additional active oxygen intermediate (OO*).

We find that these kinetic features, however, can in fact be rationalized by invoking the presence of a dissociatively adsorbed oxygen pool - distinct from lattice oxygens formed in irreversible dissociative adsorption steps – and present in quasi-equilibrium with gas phase oxygen, that abstract hydrogens from ethoxide intermediates formed on lattice oxygens (Scheme 2d); implicit in this reaction scheme is the assumption that the oxygen pool present in quasi-equilibrium with gas phase oxygen (represented as O**) is involved exclusively in total oxidative turnovers producing CO_x, but not partial oxidative turnovers producing ethene; lattice oxygens (represented as O*) formed through irreversible dissociative adsorption steps, on the other hand, are involved in hydrogen abstraction events common to both catalytic cycles. The following steps comprise these proposed catalytic cycles (Table 2): the quasi-equilibrated adsorption of ethane onto lattice oxygen (O*) (step 1), the irreversible abstraction of hydrogen by a neighboring lattice oxygen (step 2), ethene desorption through ß-hydride elimination (step 3), followed by irreversible recombinative water desorption (step 5) and dissociative oxygen adsorption (step 6) steps that regenerate lattice oxygen sites and close out the ethene formation catalytic cycle. Whereas hydrogen/hydride elimination from lattice oxygen-derived ethoxide intermediates result in ethene formation (step 3), carbon–oxygen bond formation steps involving these lattice oxygen-derived ethoxide intermediates and O** species (step 4) are postulated to precede a series of irreversible steps that result in CO_x formation. O** species are generated through the quasi-equilibrated dissociative adsorption of oxygen on ** sites (step 7), the identity of which remain beyond the scope of this work, and remain inaccessible given the limited kinetic techniques applied in this study. $MoVTeNbO_x$ catalysts used here carry not only multiple phases but also metals within each phase that exist in a variety of oxidation states [72,73], and present a multitude of possibilities for potential oxygen adsorption sites. Claims abound in the open literature as to the involvement of electrophilic and nucleophilic oxygen species on $MoVTeNbO_x$ catalysts in CO/CO_2 and olefin formation steps, respectively [2,3,45]. Heracleous and Lemonidou proposed a two oxygen-site model for ethane oxidation over Nb-doped nickel oxides - one site responsible for ethane oxidative dehydrogenation and ethene secondary oxidation, and another that catalyzes total oxidation of ethane [53,74]. Rahman et al. employed two-site models combining Eley-Rideal and redox mechanisms for capturing trends in ethane oxidation performance over MoV type catalysts [75]. We invoke the existence of a quasi-equilibrated oxygen pool that is involved in oxygen insertion steps leading to CO_x formation; this oxygen pool does not participate in ethene partial oxidative turnovers producing ethene, which instead involve exclusively a single type of lattice oxygen species formed in irreversible dissociative adsorption steps. We emphasize the fact that no claims as to the identity or electrophilicity of these active oxygen species, or in fact even the nature of sites that enable dissociative adsorption of oxygen in the first place are made in our interpretation of the presented kinetic data.

Table 2
Proposed sequence of elementary steps for the oxidation of ethane to ethene and CO_x over $MoVTeNbO_x$ catalysts. The rates of each of the corresponding elementary steps are shown on the right with rate parameters for steps involving multiple sites being apparent rate parameters that include the corresponding coordination numbers.

Step	Reaction	Equation
1	$C_2H_6 + O^* \leftrightarrow^{K_1} C_2H_6O^*$	$[C_2H_6O^*] = K_1[C_2H_6][O^*]$
2	$C_2H_6O^* + O^* \overset{k_2}{\rightarrow} C_2H_5O^* + OH^*$	$r_2 = k_2[C_2H_6O^*][O^*]$
3	$C_2H_5O^* \overset{k_3}{\rightarrow} C_2H_4 + OH^*$	$r_3 = k_3[C_2H_5O^*]$
4	$C_2H_5O^* + O^{**} \overset{k_4+O^{**}-OH^{**}}{\longrightarrow} CO_x* + CO_x + **$	$r_4 = k_4[C_2H_5O^*][O^{**}]$
5	$2OH^* \overset{k_5}{\rightarrow} H_2O + O^* + *$	$r_5 = k_5[OH^*]^2$
6	$O_2 + 2* \overset{k_6}{\rightarrow} 2O^*$	$r_6 = k_6[O_2][*]^2$
7	$O_2 + 2** \leftrightarrow^{K_7} 2O^{**}$	$[O^{**}] = K_7[O_2][**]^2$

O* represents a lattice oxygen formed through irreversible dissociative oxygen adsorption, O** represents dissociatively adsorbed oxygen present in quasi-equilibrium with gas phase oxygen, OH* represents a surface hydroxyl, * represents a lattice oxygen vacancy, and ** represents an adsorption site for quasi-equilibrated oxygen adsorption.

The sequence of elementary steps listed in Table 2, conditional on steps 1 and 7 being quasi-equilibrated, and upon application of the pseudo-steady state assumption to *, OH^* and $C_2H_5O^*$ intermediates leads to the following expression for the rate of ethene formation (derivation in section S11, SI):

$$r_1 = \frac{k_2K_1[C_2H_6]}{\left(1 + K_1[C_2H_6] + \sqrt{\frac{k_2K_1[C_2H_6]}{k_5}} + \sqrt{\frac{k_2K_1[C_2H_6]}{2k_6[O_2]}}\right)^2}, \quad (11)$$

O^* $C_2H_6O^*$ OH^* *

where K2 is the rate constant for C–H bond activation, K_1 is the equilibrium constant for ethane adsorption, k_5 is the rate constant for recombinative water desorption, and k_6 the rate constant for reoxidation of reduced sites. Terms in the denominator represent (in order of appearance) $C_2H_6O^*$, OH^* and * coverages relative to those of O*. Water inhibition terms are absent in the denominator of the rate expression as a consequence of the irreversible nature of recombinative water desorption steps (step 5, Table 2), and are consistent with negligible effects of water co-feeds and residence times on ethene formation rates (section 4.2). Significant coverages of adsorbed ethane would be expected to lead not only to a lack of sensitivity of rates to ethane pressures but an inhibitory effect of ethane on ODHE rates at sufficiently high pressures; such inhibitory regimes are not accessed in the experiments reported here, suggesting a negligible contribution of these species to the overall site balance. Model fits described in section 4.4 suggest hydroxyl coverages that are 4 orders of magnitude smaller than those of lattice oxygens and oxygen vacancies (Section S13, SI), and the inclusion of hydroxyl coverage terms lead to imperceptible improvements in the quality of rate regression, leading us to ignore their contributions to the ethane oxidation rate expression. Moreover, rates that approach first order behavior in ethane at sufficiently high oxygen pressures (~50 kPa) are indicative of negligible surface coverage contributions of hydroxyls and adsorbed ethane, the magnitude of both of

which are determined solely by the ethane pressure under consideration. Steady state contributions of reduced site coverages, on the other hand, are instead determined by a balance between the rates of lattice oxygen consumption in hydrogen abstraction steps and those of oxygen generation through dissociative adsorption steps (steps 2 and 6, Table 2), and hence are a function of the ethane to oxygen molar ratio, and offer a plausible basis for explaining rate dependencies reported in Fig. 3. Rates are not only first order in ethane at sufficiently low ethane pressures but also independent of oxygen pressure as a result of the existence of predominantly empty surfaces comprised of exposed lattice oxygens involved in ethane adsorption and C–H bond scission; at these low ethane pressures, oxygen pressures tested in this study (10–50 kPa), and hence oxygen adsorption rates, are sufficient to maintain a predominantly oxidized surface reflected in first order rate behavior in ethane. Deviations from first order behavior, however, are observed at higher ethane pressures where these same oxygen pressures can result in finite reduced site coverages owing to the much larger rates at which lattice oxygens activate ethane. The higher rates of hydrogen abstraction associated with these higher ethane pressures also results in greater sensitivities to oxygen pressure (Fig. 3b); rates are first order in oxygen at 50 kPa ethane and low oxygen pressures, and transition to zero order behavior at higher oxygen pressures that result in fully O* covered surfaces. These predominantly O* covered surfaces are accessed, and concomitant zero order behavior in oxygen observed, at progressively lower oxygen pressures with decreasing ethane pressure (50–25-10 kPa), consistent with ethane to oxygen ratios, not merely either oxygen or ethane pressures, determining relative coverages of reduced sites and hydroxyls, respectively. Trends in Fig. 3 can be captured quantitatively using the following simplified rate expression in which contributions of adsorbed ethane and hydroxyl species are assumed to be negligible:

$$r_1 = \frac{k_2 K_1 [C_2H_6]}{\left(1 + \sqrt{\frac{k_2 K_1 [C_2H_6]}{2k_6 [O_2]}}\right)^2} \tag{12}$$

This rate expression can be recast in an equivalent form (Eq. (13)) by combining the product of k_2 and K_1 to be represented by k', and k_6 represented instead for convenience as k_0 – the rate constant for re-oxidation of lattice oxygen vacancies - since k_6 is used to represent the apparent rate constant for the CO oxidation step (step 6) in the reaction network:

$$r_1 = \frac{k' [C_2H_6]}{\left(1 + \sqrt{\frac{k' [C_2H_6]}{2k_o [O_2]}}\right)^2}. \tag{13}$$

We note that Annamalai et al. [65] noted first order dependency on ethane and zero order dependency on oxygen at least in part due to the higher temperatures (648–733 K) and smaller range of reactant pressures (P_{ethane} = 1–8 kPa and P_{oxygen} = 1–15 kPa) used in their study. The significantly greater reactant pressures (P_{ethane} = P_{oxygen} = 0–500 kPa) used in our study, as well as lower temperature (603 K) measurements enabled by the use of H_2O_2-mediated selective phase dissolution procedures applied herein allow us to identify non-first and zero order behavior in ethane and oxygen, respectively, and to eliminate more simplistic mechanistic proposals presented in our previous study that explain high-temperature, low-pressure rate features with sufficient levels of accuracy [38].

We invoke a dissociatively adsorbed oxygen species (O**) present in quasi-equilibrium with gas phase oxygen that is involved in CO_x, but not ethene formation. Applying the pseudo-steady state hypothesis to $C_2H_5O^*$, OH^*, and* intermediates, and assuming step 4 to be rate determining in the case of ethane total oxidation to CO_x, the sequence of steps presented in Table 2 allow us to derive the following rate expression for CO_x formation (derivation in section S11, SI):

$$r_{2,3} = \frac{2\frac{k_2 k_4 K_1}{k_3}[C_2H_6]}{\left(1 + K_1[C_2H_6] + \sqrt{\frac{k_2 K_1 [C_2H_6]}{k_5}} + \sqrt{\frac{k_2 K_1 [C_2H_6]}{2k_6 [O_2]}}\right)^2} \frac{\sqrt{K_7[O_2]}}{1+\sqrt{K_7[O_2]}}, \tag{14}$$

O^* $C_2H_6O^*$ OH^* $*$

where terms in the denominator term on the left hand side represent $C_2H_6O^*$,$OH^*$and * coverages relative to O*. In cases where the oxygen adsorption equilibrium constant is small enough where ** surfaces are mostly uncovered, i.e. $\sqrt{K_7[O_2]} \ll 1$, Eq. (14) can be simplified to the following form:

$$r_{2,3} = \frac{2\frac{k_2 k_4 K_1}{k_3}[C_2H_6]}{\left(1 + K_1[C_2H_6] + \sqrt{\frac{k_2 K_1 [C_2H_6]}{k_5}} + \sqrt{\frac{k_2 K_1 [C_2H_6]}{2k_6 [O_2]}}\right)^2} \sqrt{K_7[O_2]}. \tag{15}$$

From Eqs. (11) and (15), the ratio of the rates of ethane total to partial oxidation can be expressed as:

$$\frac{r_1}{r_{2,3}} = \frac{\frac{k_3}{2k_4}}{\sqrt{K_7[O_2]}}. \tag{16}$$

Assuming $C_2H_6O^*$, OH^*, and * coverages are much smaller than those of O^*, Eq. (15) can be further simplified to the following form:

$$r_i = k_i'' [C_2H_6]\sqrt{K_7[O_2]}, \tag{17}$$

where the k_i'' is the rate constant for the deep oxidation of ethane (step 2 and step 3 combined). This simplified rate expression that assumes predominantly uncovered O* and ** surfaces was found to capture rate dependencies reported in Fig. 4, due in part to the higher temperatures (643 K) and smaller range of ethane (20–155 kPa) and oxygen (10–100 kPa) pressures covered compared to those used to develop rate expressions for ethene formation (0–500 kPa oxygen and ethane, Fig. 3). We emphasize here the fact that higher temperatures are required for the quantification of CO_x formation rates with meaningful levels of accuracy, and that the pressure ranges over which these total oxidation rates can be reported are somewhat limited due to the prohibitively large conversion-scaled adiabatic temperature rise values and resulting temperature gradients at higher pressures. Steps postulated in Table 2 and the assumptions used in deriving Eqs. (11) and (15) also lead to an accurate description of ethane partial to total oxidation rate ratios at 643 K that are weakly dependent on ethane pressure but exhibit negative half order dependency on oxygen pressure (Figure S6B, SI) - dependencies that are challenging to reconcile using sequences that exclusively involve lattice oxygen despite accounting for inner and outer sphere routes for surface reoxidation (Schemes 2a-c).

Proposed sequences for ethene and CO_x formation are also consistent with kinetic isotope effects (KIEs) reported in Table 3 that were assessed by feeding C_2H_6/O_2 and C_2D_6/O_2 mixtures under conditions leading to sub-10% ethane conversion at 623, 643, and 663 K, and rate constants at

Table 3
Kinetic isotope effects for ethane oxidation over $MoVTeNbO_x$ catalysts measured by feeding C_2H_6/O_2 and C_2D_6/O_2 mixtures; reaction conditions: 623–663 K, 12 kPa C_2H_6/C_2D_6, 6 kPa O_2, 45 sccm total flow at atmospheric pressure. $k_{1,C-H/C-D}$ represents the ratio of first order apparent rate constants k_2K_1, $k_{2,C-H/C-D}$ and $k_{3,C-H/C-D}$ represent the ratios of k_2'' and k_3'' in Eq. (17), respectively.

Temperature (K)	Dehydrogenation	Deep oxidation	
	$k_{1,C-H/C-D}$	$k_{2,C-H/C-D}$	$k_{3,C-H/C-D}$
623	3.79	1.07	1.09
643	3.56	1.03	0.96
663	3.48	1.09	1.28

these three temperatures back calculated using Eq. (12). KIE values for ethene formation from ethane - reported here as the ratio of apparent rate constants (k_2K_1) - were found to range between 3.4 and 3.8, and those for CO_x formation from ethane were found to range between 0.96 and 1.28, consistent with the kinetic relevance of C–H scission steps in the former (step 2, Table 2) and the rate determining nature of either C-O bond formation or C–C bond scission steps in the latter (step 4, Table 2). The kinetic relevance of C–H bond scission steps toward ethene formation noted here align with proposals in the prior literature for ethane partial oxidation over supported vanadia and molybdenum, as well as bulk $MoVTeNbO_x$ catalysts [27,45,65,76–79]. Specifically, a KIE value of 2.4 was reported by the Iglesia group for ethene formation over supported vanadia catalysts [27] and a value of 2.4–2.9 reported by the Lemonidou group for bulk nickel oxide catalysts [80]. C_2H_6/C_2D_6 rate ratios for CO_x formation that deviate from unity, on the other hand, are not that commonly reported in the literature. Yao et al. reported near-identical rates for C_2H_4 and C_2D_4 oxidation over bulk nickel oxide catalysts, and proposed that scission of the carbon–carbon double bond constitutes the rate determining step for ethene oxidation [81]. In contrast with isotopic data on the $MoVTeNbO_x$ catalyst reported here, Argyle et al. postulated C–H activation to be kinetically relevant for the total oxidation of ethane as well as the oxidation of ethene over supported vanadia catalysts, and reported rate constant ratios of 1.9 and 2.8, respectively, for these two reactions [27]. The kinetically demanding nature of carbon–carbon bond scission/oxygen insertion steps over $MoVTeNbO_x$ catalysts studied here and the associated lack of kinetic relevance of C–H scission steps may provide hints as to the basis for the significantly greater selectivities of M1 phase oxides compared to supported vanadia catalysts, the latter of which appear to carry C-O bond formation/C–C bond scission steps that are not sufficiently kinetically demanding as to result in kinetically irrelevant hydrogen abstraction steps. The precise basis for the exceptionally high ethene selectivities of M1 phase materials considered here, as well as those evaluated more broadly in the literature remain speculative at best, and will constitute the focus of future investigations.

4.3.2. Ethene and CO oxidation kinetics

Product inhibition effects appear to contribute negligibly toward measured ethene oxidation rates (steps 4,5, and 6, Scheme 1), as evidenced using co-feed experiments described in section 4.2. CO and CO_2 formation rates at 663 K both exhibit first order dependency in ethene (5–100 kPa, Fig. 5a) and half order dependency on oxygen (5–480 kPa, Fig. 5b). Ethene conversions were maintained below 1.8% to minimize contributions of CO oxidation to measured CO_2 formation rates. Ethene oxidation rate data can be represented using the following power law rate expression:

$$r_i = k_i[C_2H_4][O_2]^{1/2} \tag{18}$$

where k_i represents the corresponding apparent rate constant for ethene oxidation to either CO or CO_2. The utility of this rather simple empirical rate expression, the mechanistic basis for which we do not seek to establish both due to the abundance of mechanistic possibilities as well as the limited nature of the kinetic data available, is exaggerated in our study due to the significantly smaller range of ethene pressures (compared to ethane pressures) encountered in the vast majority of kinetic measurements reported.

Co-feed experiments reported in section 4.2 are suggestive of the non-negligible nature of CO oxidation pathways in determining CO_2 formation rates. Kinetic models reported in the prior literature, however, exclude CO oxidation steps [32,45] despite reports asserting its plausibility over metal [82], metal oxide [83,84], and Pd-containing $MoVTeNbO_x$ catalysts [85,86]. CO oxidation rates at 683 K, analogous to ethene oxidation rates, were found to be first order in CO and half order in oxygen (Fig. 6), analogous to reaction orders reported over La_2O_3/CaO catalysts between 900 and 1200 K by Stansch et al. [87]. CO oxidation rates can therefore be expressed as:

$$r_i = k_6[CO][O_2]^{1/2} \tag{19}$$

where k_6 is the apparent rate constant for ethene oxidation. Having obtained forms of rate expressions for each of the 6 steps in the reaction network, we now estimate model kinetic parameters by regressing to experimentally measured rate data.

4.4. Global kinetic model parameter estimation

Table 4 lists rate expressions constituting the proposed global kinetic model used to describe ethane oxidation rate data over the $MoVTeNbO_x$ catalyst under consideration. Rate expressions for primary partial and deep oxidation reactions (steps 1–3, Scheme 1) are derived from specific sequences of elementary steps described in section 4.3, whereas those for secondary reactions (steps 4–6, Scheme 1) are empirical in nature due in part to the smaller range of reactant partial pressures of relevance. Rates of all undesired reactions were assumed to be first order in hydrocarbon/oxygenate and half order in oxygen, consistent with the experimental data reported in section 4.3. We emphasize in our approach the use of the least number of fitting parameters that explain the entirety of the differential and integral kinetic features reported in

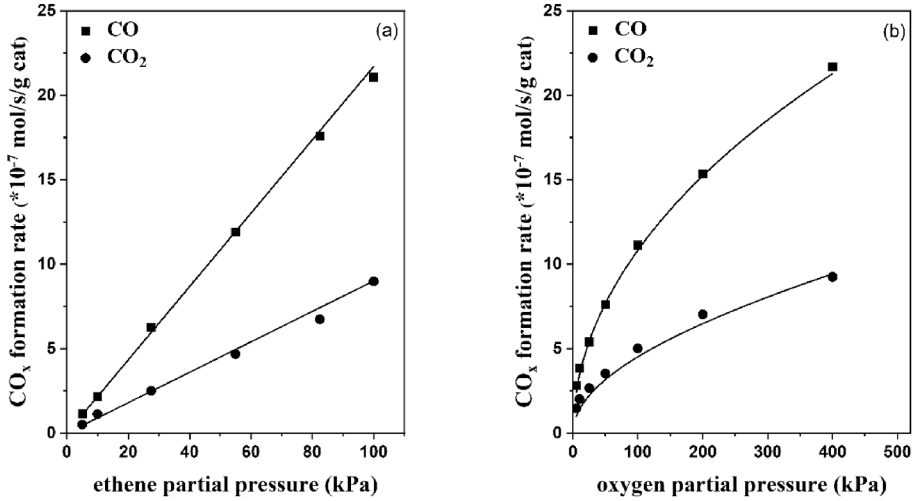

Fig. 5. Effect of (a) ethene partial pressure at 25 kPa O_2 and (b) O_2 partial pressure at 25 kPa ethene on CO_x formation rates over 100 mg $MoVTeNbO_x$ at 663 K with He as inert, and 6 bar total pressure, 120 sccm total flow at atmospheric pressure. Solid lines represent model predictions and symbols represent experimental data.

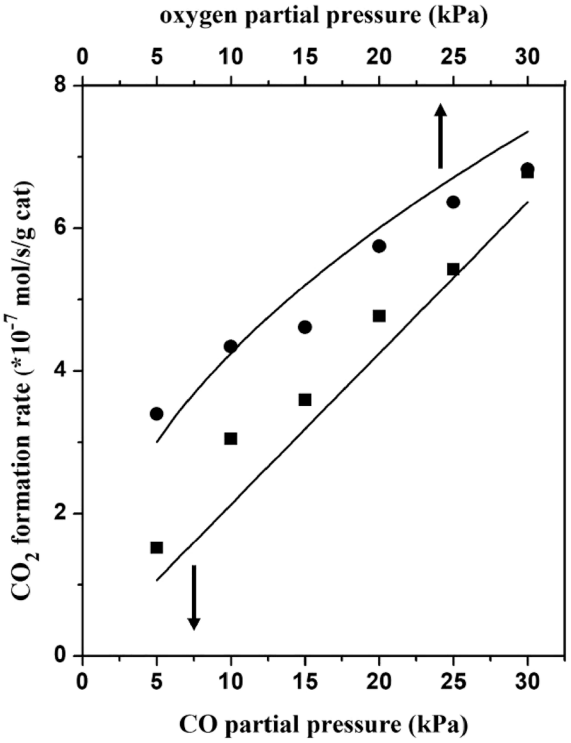

Fig. 6. Effect of CO pressure (squares) at 10 kPa oxygen, and oxygen pressure (circles) at 20 kPa CO, on CO_2 formation rates over 0.1 g $MoVTeNbO_x$ at 683 K with He as inert at 6 bar total pressure. Solid lines represent model predictions and symbols represent experimental data.

Table 4
Global kinetic model rate expressions used to describe ethane oxidation rate data over $MoVTeNbO_x$ (603–703 K, P_{C2H6}/P_{O2}: 5–480 kPa, contact time: 0.04–1.5 s).

Reaction steps	Rate expression
$R1: C_2H_6 + 0.5O_2 \rightarrow C_2H_4 + H_2O$	$r_1 = \frac{k_1'[C_2H_6]}{\left(1+\sqrt{\frac{k_1'[C_2H_6]}{2k_o[O_2]}}\right)^2}$
$R2: C_2H_6 + 2.5O_2 \rightarrow 2CO + 3H_2O$	$r_2 = k_2[C_2H_6][O_2]^{0.5}$
$R3: C_2H_6 + 3.5O_2 \rightarrow 2CO_2 + 3H_2O$	$r_3 = k_3[C_2H_6][O_2]^{0.5}$
$R4: C_2H_4 + 2O_2 \rightarrow 2CO + 2H_2O$	$r_4 = k_4[C_2H_4][O_2]^{0.5}$
$R5: C_2H_4 + 3O_2 \rightarrow 2CO_2 + 2H_2O$	$r_5 = k_5[C_2H_4][O_2]^{0.5}$
$R6: CO + 0.5O_2 \rightarrow CO_2$	$r_6 = k_6[CO][O_2]^{0.5}$

this study. A regression analysis of all collected differential steady state data was used to obtain values of kinetic model parameters, with experimentally determined apparent activation energy values (section S14, SI) serving as initial guesses. These kinetic parameters, i.e. pre-exponential factors and apparent activation energies, which were further validated using integral measurements, along with their corresponding 90% confidence intervals are listed in Table 5.

Partial oxidation of ethane (step 1, Scheme 1) was found to exhibit the lowest apparent activation energy of all steps in the reaction network except for CO oxidation (step 6, Scheme 1), with the estimated value - 89.4 kJ/mol - being not dissimilar to values reported by the Deshlahra group over $MoVTeNbO_x$ catalysts not treated in H_2O_2 (79 kJ/mol) [65] and the de Lasa group over alumina-supported vanadia catalysts (88.3 kJ/mol) [88]. Apparent activation energies for ethane oxidation to CO_x (steps 2 and 3, Scheme 1) that are 40–50 kJ/mol greater than those corresponding to its partial oxidation to ethene, taken together with non-unitary values of C_2H_6/C_2D_6 kinetic isotope effects for ethene formation but not CO_x formation, suggest that apparent activation energies for the latter, unlike the former, sense enthalpy changes not merely of

Table 5
Estimated pre-exponential factors, apparent activation energies, their associated 90% confidence intervals, and corresponding apparent activation energy values reported in the literature.

Reaction steps	$k_{0,i}$ (mol/s/g_{cat}/kPa^m)	$E_{a,j}$ (kJ/mol)	$E_{a,j}$/literature (kJ/mol)
1	3.59 ± 0.57	89.4 ± 3.7	88.3 [88], 79 [65]
	490.4 ± 430.8	101.6 ± 5.1	118.3 [90]
2	39.37	138.4	156.5 ± 30.2 [33]
3	17.59	130.7	122.7 ± 16.6 [33]
4	7.31 ± 4.28	120.8 ± 4.4	109 ± 3 [32]
5	3.69 ± 2.77	122.1 ± 9.3	120 ± 4 [32]
6	7.36E-5 ± 3.96E-5	52.8 ± 3.2	45 [91], 71 [92]

The first row of step 1 represents k' and the second row of step 1 represents k_o (both in Eq. (13)). m = 1 for step 1 and m = 1.5 for steps 2–6. Confidence intervals for steps 2 and 3 are not reported due to the lack of access to error bars challenging to access at extremely low ethane conversions.

C–H bond scission transition states relative to uncovered surfaces but also possibly C–C bond scission/C-O bond formation steps that are kinetically more demanding in nature. Identical surface coverages and kinetically relevant transition states for partial and deep oxidation sequences should lead to *both* non-unitary KIE values as well as identical apparent activation energies - values that clearly differ for ethane partial and deep oxidation. The greater temperature sensitivities of ethane total oxidation rates compared to partial oxidation rates reinforce the need for tight temperature control within industrially viable reactor configurations, and evidence the need for global models that rigorously capture total oxidation kinetics so as to facilitate accurate modeling of rate features in highly non-isothermal reactors [38,89]. Secondary ethene oxidation steps to produce CO and CO_2 were found to carry apparent activation energies of 120.8 and 122.1 kJ/mol, respectively, similar to values of 109 kJ/mol and 120 kJ/mol reported by Che-Galicia et al. for these two steps [36].

198 independent kinetic experiments were used to develop the kinetic model presented here. Model fits toward experimentally measured differential data are shown in Figs. 3-6 and in section S17 of the Supporting Information. Not only does the model capture a range of features within these differential data but also explains effects of contact time on ethane/oxygen conversion and ethene/CO/CO_2 selectivity in integral data measured between 613 and 653 K- effects that are captured sufficiently well using a 1D pseudo-homogeneous PFR model (Fig. 7). Heat transfer rates have to necessarily be included when describing integral data presented here due to large adiabatic temperature rise values (600–1000 K) that render beds highly non-isothermal. Conversions increase supra-linearly with contact time when values of the latter are low enough as to be comparable to heat loss time scales (of the order of 60 ms), but less sensitively as contact times significantly exceed heat loss time scales, thereby resulting in reactor behavior that more closely approaches isothermal behavior, and conversions that increase close to linearly with contact time (Fig. 7a).

Parity plots that compare experimentally measured rates and product mole fractions with model predicted values evidence (for the most part) agreement between the two within an accuracy of ± 20% (Fig. 8). Model descriptions of differential features (Fig. 8a-c, average deviation: 10.7%) were found to be marginally more accurate compared to those for integral measurements (Fig. 8e-f, average deviation: 13.1%). The 1D pseudo-homogeneous PFR models used in this study ignores contributions of heat conduction through the catalyst bed, with an average heat Peclet number value of around 10 suggesting minor but non-negligible extents of thermal back-mixing; finite heat dispersion models that more rigorously capture heat loss and conduction rates will help further refine model predictions, and will be explored as part of our future work. The reasonable agreement observed between model predictions and experimental data despite the wide range of reactant pressures, contact times, and reaction temperatures tested point to the utility of the

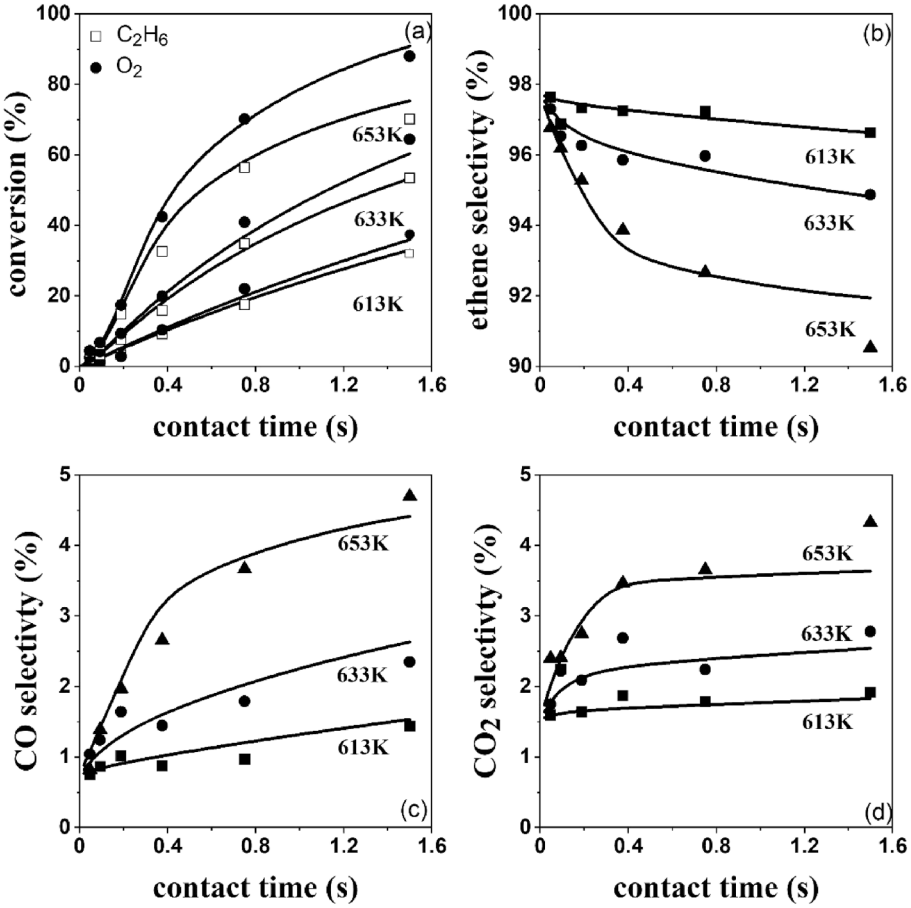

Fig. 7. (a) Ethane and oxygen conversion (b) ethene selectivity (c) CO selectivity (d) CO_2 selectivity as a function of contact time in the presence of 20 kPa ethane and 10 kPa oxygen. Solid lines represent model predictions and symbols represent experimental data.

presented model in the comparative design of non-isothermal reactors, the viability of which are strongly dependent on kinetic and thermodynamic behavior of highly exothermic side reactions. Especially important in this respect is the fact that this model - applicable over a wide range of reaction conditions - lends itself amenable to application in the calculation of bifurcation diagrams that help map out feasible regions for autothermal operation.

5. Conclusions

We report herein a global kinetic model that describes (with reasonable accuracy) differential and integral $MoVTeNbO_x$-catalyzed ethane oxidation rate behavior over a wide range of reaction conditions – 603–703 K, P_{C2H6}/P_{O2}: 5–480 kPa, contact time: 0.04–1.5 s. The greater ethane to oxygen molar ratios accessible in measurements at supra-ambient pressures result in non-negligible coverages of reduced centers and concomitant positive fractional order rate sensitivities to oxygen observed at either sufficiently high ethane pressures or adequately low oxygen pressures; these data appear to eliminate from consideration quasi-equilibrated dissociative oxygen adsorption steps that explain sufficiently well low-pressure rate data reported previously by our group [38], but not the supra-ambient pressure features reported in this study. The greater sensitivities of ethane deep oxidation rates to oxygen pressure compared to ethane partial oxidation rates can be rationalized by invoking an active oxygen pool present in quasi equilibrium with gas phase O_2; this oxygen pool is posited to be involved exclusively in oxygen insertion/C–C bond scission steps, but not C–H bond activation steps that exhibit kinetic relevance in partial oxidative turnovers producing ethene, but not total oxidative turnovers producing CO_x that instead appear to be limited by oxygen insertion/C–C bond scission steps. Product inhibition effects were concluded to be negligible under the conditions used in this study (as evidenced using a range of co-feed experiments), and empirical power law models that ignore changes in surface coverages with reaction temperature or reactant pressure and that result in first order behavior in hydrocarbon/CO and half order behavior in oxygen for undesired reactions were found to be sufficient to explain measured rate data. Rates of undesired total oxidation reactions of ethane and ethene - significantly more exothermic albeit much less prevalent over $MoVTeNbO_x$ catalysts evaluated in our experiments - were found to exhibit greater sensitivity to temperature compared to ethane partial oxidation rates, pointing to the need for tight temperature control in the industrial practice of ODHE - control that may be highly challenging to achieve using cooled multitubular reactors susceptible to hot spot formation. Parity plots point to sound agreement between model predictions and experimentally measured differential rates over a wide range of reaction conditions; integral data were also found to be predicted with sufficient accuracy despite the use of a 1D pseudo-homogenous PFR model that ignores heat conduction through the catalyst bed. An abundance of merits of this nature render the kinetic model presented herein to be ideally suited for the purposes of mapping bifurcation behavior, as well as evaluating the feasibility of autothermal operation as a function of reaction variables. The model addresses key gaps in the ODHE literature, including considerations relating to high-pressure operation and the prevalence of undesired reactions, thereby proving a foundation for meaningful reactor design studies for ODHE – investigations critical to the scale up and commercialization of catalytic oxidative routes for natural gas valorization more broadly.

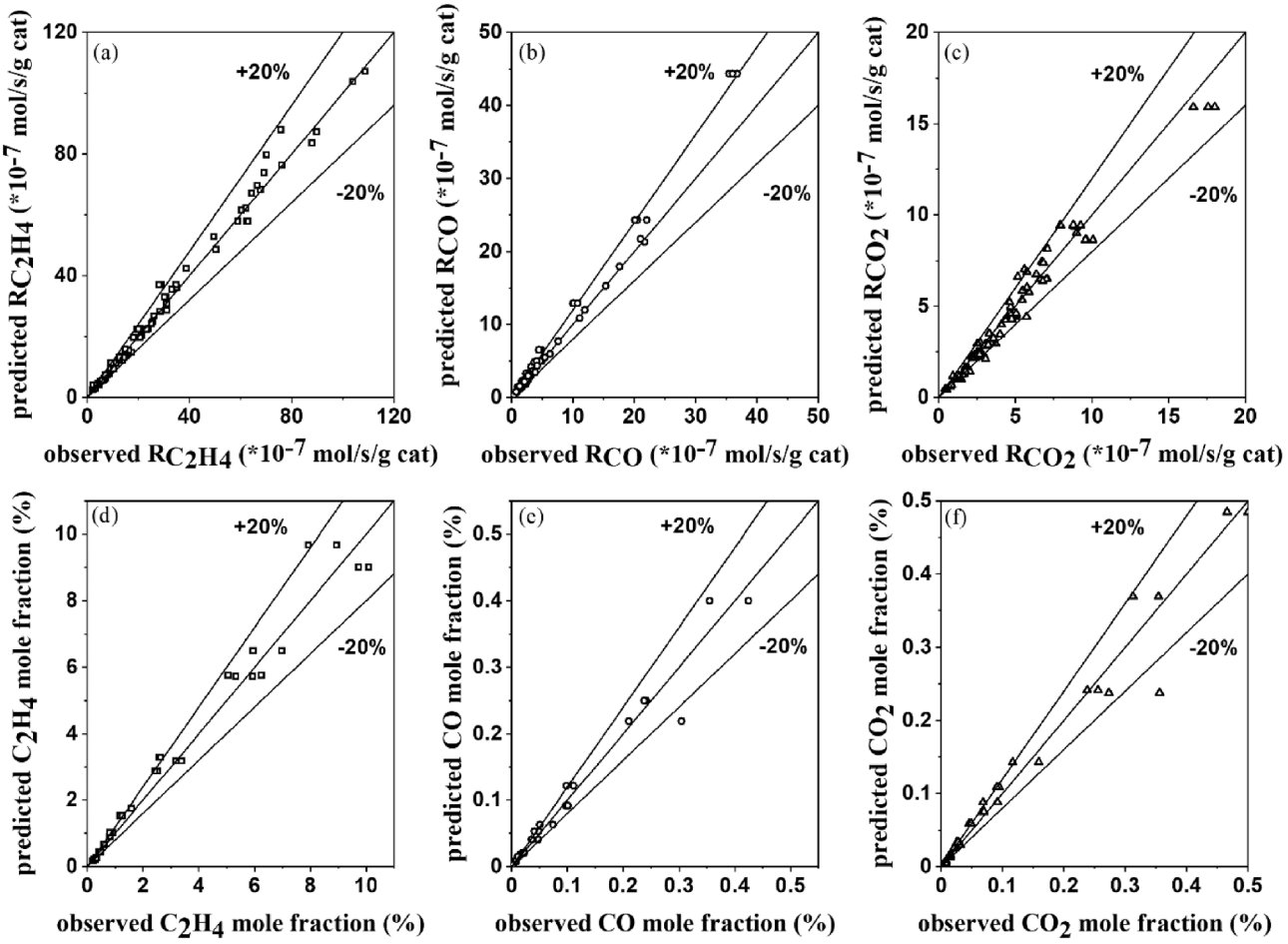

Fig. 8. Parity plots of experimental and calculated (a) ethene formation rates (b) CO formation rates (c) CO_2 formation rates (d) outlet ethene mole fraction (e) outlet CO mole fraction (f) outlet CO_2 mole fraction; figures a-c report differential measurements, and figures d-f report integral measurements.

Declaration of Competing Interest

The authors declare that they have no known competing financial interests or personal relationships that could have appeared to influence the work reported in this paper.

Acknowledgements

This work was supported by funding from the National Science Foundation (Grant # CBET-2133174). The authors acknowledge technical discussions with David West and Pankaj Gautam from SABIC that helped shape some of work described in this manuscript. PB acknowledges helpful technical discussions with Professor Enrique Iglesia relating to reoxidation pathways and oxygen speciation in the context of bulk oxide-mediated catalytic partial oxidation reactions.

Appendix A. Supplementary data

Supplementary data to this article can be found online at https://doi.org/10.1016/j.cej.2022.136605.

References:

[1] F. Cavani, N. Ballarini, A. Cericola, Oxidative dehydrogenation of ethane and propane: How far from commercial implementation? Catal. Today. 127 (2007) 113–131, https://doi.org/10.1016/j.cattod.2007.05.009.

[2] C.A. Gärtner, A.C. vanVeen, J.A. Lercher, Oxidative dehydrogenation of ethane: Common principles and mechanistic aspects, ChemCatChem 5 (2013) 3196–3217, https://doi.org/10.1002/cctc.201200966.

[3] J.T. Grant, J.M. Venegas, W.P. McDermott, I. Hermans, Aerobic oxidations of light alkanes over solid metal oxide catalysts, Chem. Rev. 118 (2018) 2769–2815, https://doi.org/10.1021/acs.chemrev.7b00236.

[4] Z. Zhang, G. Zhao, Y. Liu, Y. Lu, High-performance Ni-foam-structured Nb_2O_5–NiO nanocomposite catalyst for oxidative dehydrogenation of shale gas ethane to ethylene: Effects of Nb_2O_5 loading and calcination temperature, Microporous Mesoporous Mater. 288 (2019), 109609, https://doi.org/10.1016/j.micromeso.2019.109609.

[5] A.M. Gaffney, O.M. Mason, Ethylene production via oxidative dehydrogenation of ethane using M1 catalyst, Catal. Today. 285 (2017) 159–165, https://doi.org/10.1016/j.cattod.2017.01.020.

[6] K. Karim, H.M. Al-Hazmi, E. Mamedov, Catalysis for the oxidation of ethane to acetic acid, processes of making same and processes of using same, U.S. Patent, No.5,907,056, 1999.

[7] R.J. Schoonebeek, G. VAN ROSSUM, Alkane oxidative dehydrogenation and/or alkene oxidation, WIPO Patent, No.2020/074750 A1, 2019.

[8] J. Leonard Edward Bogan, A.M. Gaffney, S. Hann, M.D. Heffner, R. Song, Recalcined catalyst, U.S. Patent, No.6,841,699 B2, 2005.

[9] F. Borgmeier, K.J. Müller-Engel, H. Hibst, M. Dieterle, Preparation of a multimetal oxide material, U.S. Patent, No.7,038,082 B2, 2006.

[10] A.M. Gaffney, R. Ghosh, R. Song, C.Y. Yeh, T. Langner, Process for making catalysts useful for the conversion of paraffins to olefins, U.S. Patent, NO.8,105,971 B2, 2012.

[11] T. Ushikubo, K. Oshima, A. Kayou, M. Hatano, Ammoxidation of propane over Mo-V-Nb-Te mixed oxide catalysts, Stud. Surf. Sci. Catal. 112 (1997) 473–480, https://doi.org/10.1016/S0167-2991(97)80871-3.

[12] P. DeSanto, D.J. Buttrey, R.K. Grasselli, C.G. Lugmair, A.F. Volpe, B.H. Toby, T. Vogt, Structural aspects of the M1 and M2 phases in MoVNbTeO propane ammoxidation catalysts, Zeitschrift Fur Krist. 219 (2004) 152–165, https://doi.org/10.1524/zkri.219.3.152.29091.

[13] J.M. Oliver, J.M. López Nieto, P. Botella, A. Mifsud, The effect of pH on structural and catalytic properties of MoVTeNbO catalysts, Appl. Catal. A Gen. 257 (2004) 67–76. 10.1016/S0926-860X(03)00632-X.

[14] P. Beato, A. Blume, F. Girgsdies, R.E. Jentoft, R. Schlögl, O. Timpe, A. Trunschke, G. Weinberg, Q. Basher, F.A. Hamid, S.B.A. Hamid, E. Omar, L. Mohd Salim, Analysis of structural transformations during the synthesis of a MoVTeNb mixed

oxide catalyst, Appl. Catal. A Gen. 307 (2006) 137–147, https://doi.org/10.1016/j.apcata.2006.03.014.
[15] D. Melzer, G. Mestl, K. Wanninger, Y. Zhu, N.D. Browning, M. Sanchez-Sanchez, J. A. Lercher, Design and synthesis of highly active MoVTeNb-oxides for ethane oxidative dehydrogenation, Nat. Commun. 10 (2019) 1–9, https://doi.org/10.1038/s41467-019-11940-0.
[16] P. Botella, E. García-González, A. Dejoz, J.M. López Nieto, M.I. Vázquez, J. González-Calbet, Selective oxidative dehydrogenation of ethane on MoVTeNbO mixed metal oxide catalysts, J. Catal. 225 (2004) 428–438. 10.1016/j.jcat.2004.04.024.
[17] A.M. Gaffney, N.V. Duprez, K.J. Louthan, B. Borders, J. Gasque, A. Siegfried, T. G. Stanford, K.L. Roberts, Y. Alcheikhhamdona, M. Hoorfar, B. Chen, S. Majumdar, H. Murnen, Ethylene production using oxidative dehydrogenation: effects of membrane-based separation technology on process safety & economics, Catal. Today. 371 (2021) 11–28, https://doi.org/10.1016/j.cattod.2020.07.063.
[18] T.T. Nguyen, M. Aouine, J.M.M. Millet, Optimizing the efficiency of MoVTeNbO catalysts for ethane oxidative dehydrogenation to ethylene, Catal. Commun. 21 (2012) 22–26, https://doi.org/10.1016/j.catcom.2012.01.026.
[19] B. Deniau, J.M.M. Millet, S. Loridant, N. Christin, J.L. Dubois, Effect of several cationic substitutions in the M1 active phase of the MoVTeNbO catalysts used for the oxidation of propane to acrylic acid, J. Catal. 260 (2008) 30–36, https://doi.org/10.1016/j.jcat.2008.08.020.
[20] F.N. Naraschewski, A. Jentys, J.A. Lercher, On the role of the vanadium distribution in MoVTeNbO$_x$ mixed oxides for the selective catalytic oxidation of propane, Top. Catal. 54 (2011) 639–649, https://doi.org/10.1007/s11244-011-9686-x.
[21] Y. Liu, L. Annamalai, P. Deshlahra, Effects of lattice o atom coordination and pore confinement on selectivity limitations for ethane oxidative dehydrogenation catalyzed by vanadium-oxo species, J. Phys. Chem. C. 123 (2019) 28168–28191, https://doi.org/10.1021/acs.jpcc.9b07778.
[22] L. Annamalai, S. Ezenwa, Y. Dang, H. Tan, S.L. Suib, P. Deshlahra, Comparison of structural and catalytic properties of monometallic Mo and V oxides and M1 phase mixed oxides for oxidative dehydrogenation, Catal. Today. 368 (2021) 28–45, https://doi.org/10.1016/j.cattod.2020.04.046.
[23] S. Ishikawa, X. Yi, T. Murayama, W. Ueda, Heptagonal channel micropore of orthorhombic Mo_3VO_x as catalysis field for the selective oxidation of ethane, Appl. Catal. A Gen. 474 (2014) 10–17, https://doi.org/10.1016/j.apcata.2013.07.050.
[24] Y.V. Kolen'ko, W. Zhang, R.N. d'Alnoncourt, F. Girgsdies, T.W. Hansen, T. Wolfram, R. Schlögl, A. Trunschke, Synthesis of MoVTeNb oxide catalysts with tunable particle dimensions, ChemCatChem 3 (10) (2011) 1597–1606.
[25] A.C. Sanfiz, T.W. Hansen, D. Teschner, P. Schnörch, F. Girgsdies, A. Trunschke, R. Schlögl, M.H. Looi, S.B.A. Hamid, Dynamics of the MoVTeNb oxide M1 phase in propane oxidation, J. Phys. Chem. C. 114 (2010) 1912–1921, https://doi.org/10.1021/jp909352u.
[26] B. Chu, L. Truter, T.A. Nijhuis, Y. Cheng, Performance of phase-pure M1 MoVNbTeO$_x$ catalysts by hydrothermal synthesis with different post-treatments for the oxidative dehydrogenation of ethane, Appl. Catal. A Gen. 498 (2015) 99–106, https://doi.org/10.1016/j.apcata.2015.03.039.
[27] M.D. Argyle, K. Chen, A.T. Bell, E. Iglesia, Ethane oxidative dehydrogenation pathways on vanadium oxide catalysts, J. Phys. Chem. B. 106 (2002) 5421–5427, https://doi.org/10.1021/jp0144552.
[28] E. Heracleous, A.F. Lee, K. Wilson, A.A. Lemonidou, Investigation of Ni-based alumina-supported catalysts for the oxidative dehydrogenation of ethane to ethylene: Structural characterization and reactivity studies, J. Catal. 231 (2005) 159–171, https://doi.org/10.1016/j.jcat.2005.01.015.
[29] E. Heracleous, A.A. Lemonidou, Ni-Me-O mixed metal oxides for the effective oxidative dehydrogenation of ethane to ethylene - Effect of promoting metal Me, J. Catal. 270 (2010) 67–75, https://doi.org/10.1016/j.jcat.2009.12.004.
[30] M. Huff, L.D. Schmidt, Ethylene formation by oxidative dehydrogenation of ethane over monoliths at very short contact times, J. Phys. Chem. 97 (1993) 11815–11822, https://doi.org/10.1021/j100147a040.
[31] F. Donsì, K.A. Williams, L.D. Schmidt, A multistep surface mechanism for ethane oxidative dehydrogenation on Pt- And Pt/Sn-coated monoliths, Ind. Eng. Chem. Res. 44 (2005) 3453–3470, https://doi.org/10.1021/ie0493356.
[32] G. Che-Galicia, R. Quintana-Solórzano, R.S. Ruiz-Martínez, J.S. Valente, C. O. Castillo-Araiza, Kinetic modeling of the oxidative dehydrogenation of ethane to ethylene over a MoVTeNbO catalytic system, Chem. Eng. J. 252 (2014) 75–88, https://doi.org/10.1016/j.cej.2014.04.042.
[33] R. Quintana-Solórzano, G. Barragán-Rodríguez, H. Armendáriz-Herrera, J. M. López-Nieto, J.S. Valente, Understanding the kinetic behavior of a Mo-V-Te-Nb mixed oxide in the oxydehydrogenation of ethane, Fuel 138 (2014) 15–26, https://doi.org/10.1016/j.fuel.2014.07.051.
[34] J.M.L. Nieto, P. Botella, M.I. Vázquez, A. Dejoz, The selective oxidative dehydrogenation of ethane over hydrothermally synthesised MoVTeNb catalysts, Chem. Commun. (17) (2002) 1906–1907.
[35] A. de Arriba, B. Solsona, A.M. Dejoz, P. Concepción, N. Homs, P.R. de la Piscina, J. M. López Nieto, Evolution of the optimal catalytic systems for the oxidative dehydrogenation of ethane: The role of adsorption in the catalytic performance, J. Catal. (2021), https://doi.org/10.1016/j.jcat.2021.07.015.
[36] G. Che-Galicia, R.S. Ruiz-Martínez, F. López-Isunza, C.O. Castillo-Araiza, Modeling of oxidative dehydrogenation of ethane to ethylene on a MoVTeNbO/TiO_2 catalyst in an industrial-scale packed bed catalytic reactor, Chem. Eng. J. 280 (2015) 682–694, https://doi.org/10.1016/j.cej.2015.05.128.
[37] J.S. Valente, R. Quintana-Solórzano, H. Armendáriz-Herrera, G. Barragán-Rodríguez, J.M. López-Nieto, Kinetic study of oxidative dehydrogenation of ethane over MoVTeNb mixed-oxide catalyst, Ind. Eng. Chem. Res. 53 (2014) 1775–1786, https://doi.org/10.1021/ie402447h.
[38] J. Chen, P. Bollini, V. Balakotaiah, Oxidative dehydrogenation of ethane over mixed metal oxide catalysts: Autothermal or cooled tubular reactor design? AIChE J. 67 (2021) 1–13, https://doi.org/10.1002/aic.17168.
[39] H.A. Wittcoff, B.G. Reuben, J.S. Plotkin, Industrial organic chemicals, John Wiley & Sons, Third Edit, 2012.
[40] T. Ren, M. Patel, K. Blok, Olefins from conventional and heavy feedstocks : Energy use in steam cracking and alternative processes 31 (2006) 425–451, https://doi.org/10.1016/j.energy.2005.04.001.
[41] I.I. Mishanin, V.I. Bogdan, Advantages of ethane oxidative dehydrogenation on the MoVNbTeO$_x$ catalyst under elevated pressure, Mendeleev Commun. 29 (2019) 455–457, https://doi.org/10.1016/j.mencom.2019.07.034.
[42] Z. Sun, D.H. West, V. Balakotaiah, Bifurcation analysis of catalytic partial oxidations in laboratory-scale packed-bed reactors with heat exchange, Chem. Eng. J. 377 (2019) 1–17, https://doi.org/10.1016/j.cej.2018.08.151.
[43] D. Linke, D. Wolf, M. Baerns, S. Zeyß, U. Dingerdissen, Catalytic partial oxidation of ethane to acetic acid over $Mo_1V_{0.25}Nb_{0.12}Pd_{0.0005}O_x$: II. Kinetic modelling, J. Catal. 205 (2002) 32–43. 10.1006/jcat.2001.3368.
[44] S.T. Oyama, A.M. Middlebrook, G.A. Somorjai, Kinetics of ethane oxidation on vanadium oxide, J. Phys. Chem. 94 (1990) 5029–5033, https://doi.org/10.1021/j100375a049.
[45] P.J. Donaubauer, D.M. Melzer, K. Wanninger, G. Mestl, M. Sanchez-Sanchez, J. A. Lercher, O. Hinrichsen, Intrinsic kinetic model for oxidative dehydrogenation of ethane over MoVTeNb mixed metal oxides: A mechanistic approach, Chem. Eng. J. 383 (2020), 123195, https://doi.org/10.1016/j.cej.2019.123195.
[46] D. Best, B.W. Wojciechowski, On identifying the primary and secondary products of the catalytic cracking of cumene, J. Catal. 47 (1977) 11–27, https://doi.org/10.1016/0021-9517(77)90145-2.
[47] T.M. John, B.W. Wojciechowski, On identifying the primary and secondary products of the catalytic cracking of Neutral Distillates, J. Catal. 37 (1975) 240–250, https://doi.org/10.1016/0021-9517(77)90145-2.
[48] L. Bui, R. Chakrabarti, A. Bhan, Mechanistic Origins of Unselective Oxidation Products in the Conversion of Propylene to Acrolein on $Bi_2Mo_3O_{12}$, ACS Catal. 6 (2016) 6567–6580, https://doi.org/10.1021/acscatal.6b01830.
[49] M. Müller, M. Kutscherauer, S. Böcklein, G. Mestl, T. Turek, On the importance of by-products in the kinetics of n-butane oxidation to maleic anhydride, Chem. Eng. J. 401 (2020), 126016, https://doi.org/10.1016/j.cej.2020.126016.
[50] D.E. Self, J.D. Oakes, M.G. White, Selective propylene oxidation over a copper-tin oxide catalyst, AIChE J. 29 (1983) 625–631, https://doi.org/10.1002/aic.690290416.
[51] K. Chen, E. Iglesia, A.T. Bell, Kinetic isotopic effects in oxidative dehydrogenation of propane on vanadium oxide catalysts, J. Catal. 192 (2000) 197–203, https://doi.org/10.1006/jcat.2000.2832.
[52] R. Yao, J.E. Herrera, L. Chen, Y.H.C. Chin, Generalized Mechanistic Framework for Ethane Dehydrogenation and Oxidative Dehydrogenation on Molybdenum Oxide Catalysts, ACS Catal. 10 (2020) 6952–6968, https://doi.org/10.1021/acscatal.0c01073.
[53] E. Heracleous, A.A. Lemonidou, Ni-Nb-O mixed oxides as highly active and selective catalysts for ethene production via ethane oxidative dehydrogenation. Part II: Mechanistic aspects and kinetic modeling, J. Catal. 237 (2006) 175–189. 10.1016/j.jcat.2005.11.003.
[54] X. Zhao, M.D. Susman, J.D. Rimer, P. Bollini, Tuning selectivity in nickel oxide-catalyzed oxidative dehydrogenation of ethane through control over non-stoichiometric oxygen density, Catal, Sci. Technol. 11 (2021) 531–541, https://doi.org/10.1039/d0cy01732a.
[55] P. Zhao, Z.; Ning, Q.; Grabow, L. C.; Rimer, J. D.; Bollini, Analysis of (side) Product Inhibition in the Measurement of Reaction Rates in Packed-Bed Flow Reactors: The Case of Ethane Partial Oxidation, Unpubl. Results. (n.d.).
[56] H.L. Wan, X.P. Zhou, W.Z. Weng, R.Q. Long, Z.S. Chao, W. De Zhang, M.S. Chen, J. Z. Luo, S.Q. Zhou, Catalytic performance, structure, surface properties and active oxygen species of the fluoride-containing rare earth (alkaline earth)-based catalysts for the oxidative coupling of methane and oxidative dehydrogenation of light alkanes, Catal. Today. 51 (1999) 161–175, https://doi.org/10.1016/S0920-5861(99)00019-X.
[57] C. Guan, Y. Yang, Y. Pang, Z. Liu, S. Li, E.I. Vovk, X. Zhou, J.P.H. Li, J. Zhang, N. Yu, L. Long, J. Hao, A.P. van Bavel, How CO_2 poisons La_2O_3 in an OCM catalytic reaction: A study by in situ XRD-MS and DFT, J. Catal. 396 (2021) 202–214, https://doi.org/10.1016/j.jcat.2021.02.017.
[58] R.X. Valenzuela, G. Bueno, V. Cortés Corberán, Y. Xu, C. Chen, Selective oxidehydrogenation of ethane with CO_2 over CeO_2-based catalysts, Catal. Today. 61 (2000) 43–48, https://doi.org/10.1016/S0920-5861(00)00366-7.
[59] Y. Liu, A. Twombly, Y. Dang, A. Mirich, S.L. Suib, P. Deshlahra, Roles of Enhancement of C−H Activation and Diminution of C−O Formation Within M1-Phase Pores in Propane Selective Oxidation, ChemCatChem 13 (2021) 882–899, https://doi.org/10.1002/cctc.202001642.
[60] A.A. Zavitsas, The relation between bond lengths and dissociation energies of carbon-carbon bonds, J. Phys. Chem. A. 107 (2003) 897–898, https://doi.org/10.1021/jp0269367.
[61] I. Alkorta, J. Elguero, The carbon-carbon bond dissociation energy as a function of the chain length, Chem. Phys. Lett. 425 (2006) 221–224, https://doi.org/10.1016/j.cplett.2006.05.050.
[62] J.N. Michaels, D.L. Stern, R.K. Grasselli, Oxydehydrogenation of propane over Mg-V-Sb-oxide catalysts, I. Reaction network, Catal. Letters. 42 (1996) 135–137, https://doi.org/10.1007/BF00810679.

[63] J.N. Michaels, D.L. Stern, R.K. Grasselli, Oxydehydrogenation of propane over Mg-V-Sb-oxide catalysts. II. Reaction kinetics and mechanism, Catal. Letters. 42 (1996) 139–148, https://doi.org/10.1007/BF00810679.

[64] S. Gaab, J. Find, T.E. Müller, J.A. Lercher, Kinetics and mechanism of the oxidative dehydrogenation of ethane over Li/Dy/Mg/O/(Cl) mixed oxide catalysts, Top. Catal. 46 (2007) 101–110, https://doi.org/10.1007/s11244-007-0320-x.

[65] L. Annamalai, Y. Liu, S. Ezenwa, Y. Dang, S.L. Suib, P. Deshlahra, Influence of Tight Confinement on Selective Oxidative Dehydrogenation of Ethane on MoVTeNb Mixed Oxides, ACS Catal. 8 (2018) 7051–7067, https://doi.org/10.1021/acscatal.8b01586.

[66] S. Kwon, P. Deshlahra, E. Iglesia, Dioxygen activation routes in Mars-van Krevelen redox cycles catalyzed by metal oxides, J. Catal. 364 (2018) 228–247, https://doi.org/10.1016/j.jcat.2018.05.016.

[67] S. Kwon, P. Deshlahra, E. Iglesia, Reactivity and selectivity descriptors of dioxygen activation routes on metal oxides, J. Catal. 377 (2019) 692–710, https://doi.org/10.1016/j.jcat.2019.07.048.

[68] C.H. Kjaergaard, M.F. Qayyum, S.D. Wong, F. Xu, G.R. Hemsworth, D.J. Walton, N. A. Young, G.J. Davies, P.H. Walton, K.S. Johansen, K.O. Hodgson, B. Hedman, E. I. Solomon, Spectroscopic and computational insight into the activation of O_2 by the mononuclear Cu center in polysaccharide monooxygenases, Proc. Natl. Acad. Sci. U. S. A. 111 (2014) 8797–8802, https://doi.org/10.1073/pnas.1408115111.

[69] H. Basch, K. Mogi, D.G. Musaev, K. Morokuma, Mechanism of the methane → methanol conversion reaction catalyzed by methane monooxygenase: A density functional study, J. Am. Chem. Soc. 121 (1999) 7249–7256, https://doi.org/10.1021/ja9906296.

[70] J. Cho, R. Sarangi, J. Annaraj, S.Y. Kim, M. Kubo, T. Ogura, E.I. Solomon, W. Nam, Geometric and electronic structure and reactivity of a mononuclear side-on nickel (iii)-peroxo complex, Nat. Chem. 1 (2009) 568–572, https://doi.org/10.1038/nchem.366.

[71] X. Rozanska, E.V. Kondratenko, J. Sauer, Oxidative dehydrogenation of propane: Differences between N_2O and O_2 in the reoxidation of reduced vanadia sites and consequences for selectivity, J. Catal. 256 (2008) 84–94, https://doi.org/10.1016/j.jcat.2008.03.002.

[72] R. Quintana-Solórzano, I. Mejía-Centeno, H. Armendáriz-Herrera, J. Ramírez-Salgado, A. Rodríguez-Hernandez, M.D.L. Guzmán-Castillo, J.M. Lopez Nieto, J. S. Valente, Discerning the Metal Doping Effect on Surface Redox and Acidic Properties in a $MoVTeNbO_x$ for Propa(e)ne Oxidation, ACS, Omega. 6 (2021) 15279–15291, https://doi.org/10.1021/acsomega.1c01591.

[73] R.K. Grasselli, C.G. Lugmair, A.F. Volpe, Doping of MoVNbTeO (M1) and MoVTeO (M2) phases for selective oxidation of propane and propylene to acrylic acid, Top. Catal. 50 (1-4) (2008) 66–73.

[74] E. Heracleous, A.A. Lemonidou, Ni-Nb-O mixed oxides as highly active and selective catalysts for ethene production via ethane oxidative dehydrogenation. Part I: Characterization and catalytic performance, J. Catal. 237 (2006) 162–174. 10.1016/j.jcat.2005.11.002.

[75] F. Rahman, K.F. Loughlin, M.A. Al-Saleh, M.R. Saeed, N.M. Tukur, M.M. Hossain, K. Karim, A. Mamedov, Kinetics and mechanism of partial oxidation of ethane to ethylene and acetic acid over MoV type catalysts, Appl. Catal. A Gen. 375 (2010) 17–25, https://doi.org/10.1016/j.apcata.2009.11.026.

[76] T. Blasco, A. Galli, J.M. López Nieto, F. Trifiró, Oxidative dehydrogenation of ethane and n-butane on VO_x/Al_2O_3 catalysts, J. Catal. 169 (1997) 203–211, https://doi.org/10.1006/jcat.1997.1673.

[77] Z. Zhao, Y. Yamada, Y. Teng, A. Ueda, K. Nakagawa, T. Kobayashi, Selective oxidation of ethane to acetaldehyde and acrolein over silica-supported vanadium catalysts using oxygen as oxidant, J. Catal. 190 (2000) 215–227, https://doi.org/10.1006/jcat.1999.2740.

[78] E.M. Thorsteinson, T.P. Wilson, F.G. Young, P.H. Kasai, The oxidative dehydrogenation of ethane over catalysts containing mixed oxides of molybdenum and vanadium, J. Catal. 52 (1978) 116–132, https://doi.org/10.1016/0021-9517(78)90128-8.

[79] F. Cavani, F. Trifirò, Selective oxidation of light alkanes: Interaction between the catalyst and the gas phase on different classes of catalytic materials, Catal. Today. 51 (1999) 561–580, https://doi.org/10.1016/S0920-5861(99)00041-3.

[80] Z. Skoufa, E. Heracleous, A.A. Lemonidou, On ethane ODH mechanism and nature of active sites over NiO-based catalysts via isotopic labeling and methanol sorption studies, J. Catal. 322 (2015) 118–129, https://doi.org/10.1016/j.jcat.2014.11.014.

[81] Y.-F.-Y. Yao, J.T. Kummer, The oxidation of hydrocarbons and CO Over Metal Oxides, J. Catal. 3 (1973) 124–138, https://doi.org/10.1016/S1062-2896(49)80052-3.

[82] S. Ivanova, V. Pitchon, C. Petit, V. Caps, Support Effects in the Gold-Catalyzed Preferential Oxidation of CO, ChemCatChem 2 (2010) 556–563, https://doi.org/10.1002/cctc.200900302.

[83] P. Laveille, G. Biausque, H. Zhu, J.M. Basset, V. Caps, A high-throughput study of the redox properties of Nb-Ni oxide catalysts by low temperature CO oxidation: Implications in ethane ODH, Catal. Today. 203 (2013) 3–9, https://doi.org/10.1016/j.cattod.2012.05.020.

[84] S.W. Han, D.H. Kim, M.G. Jeong, K.J. Park, Y.D. Kim, CO oxidation catalyzed by NiO supported on mesoporous Al_2O_3 at room temperature, Chem. Eng. J. 283 (2016) 992–998, https://doi.org/10.1016/j.cej.2015.08.021.

[85] S.I. Al-Mayman, M.A. Soliman, A.S. Al-Awadi, Y.S. Al-Zeghayer, Reaction kinetics of ethane partial oxidation to acetic acid, Appl. Petrochemical Res. 8 (2018) 29–38, https://doi.org/10.1007/s13203-018-0195-8.

[86] M. Soliman, Y. Al-Zeghayer, A.S. Al-Awadi, S. Al-Mayman, Economics of Acetic Acid Production by Partial Oxidation of Ethane, APCBEE Procedia. 3 (2012) 200–208, https://doi.org/10.1016/j.apcbee.2012.06.070.

[87] Z. Stansch, L. Mleczko, M. Baerns, Comprehensive Kinetics of Oxidative Coupling of Methane over the La_2O_3/CaO Catalyst, Ind. Eng. Chem. Res. 36 (7) (1997) 2568–2579.

[88] S.A. Al-Ghamdi, M.M. Hossain, H.I. De Lasa, Kinetic modeling of ethane oxidative dehydrogenation over VO_x/Al_2O_3 catalyst in a fluidized-bed riser simulator, Ind. Eng. Chem. Res. 52 (2013) 5235–5244, https://doi.org/10.1021/ie303305c.

[89] S.A.R. Mulla, O.V. Buyevskaya, M. Baerns, Autothermal oxidative dehydrogenation of ethane to ethylene using $Sr_xLa_{1.0}Nd_{1.0}O_y$ catalysts as ignitors, J. Catal. 197 (1) (2001) 43–48.

[90] G.L. Dai, Z.P. Liu, W.N. Wang, J. Lu, K.N. Fan, Oxidative dehydrogenation of ethane over V_2O_5 (001): A periodic density functional theory study, J. Phys. Chem. C. 112 (2008) 3719–3725, https://doi.org/10.1021/jp075843s.

[91] I. Stará, V. Nehasil, V. Matolín, The influence of particle size on CO oxidation on Pd alumina model catalyst, Surf. Sci. 331–333 (1995) 173–177, https://doi.org/10.1016/0039-6028(95)00183-2.

[92] P. Bera, K.C. Patil, M.S. Hegde, NO reduction, CO and hydrocarbon oxidation over combustion synthesized Ag/CeO_2 catalyst, Phys. Chem. Chem. Phys. 2 (2000) 3715–3719, https://doi.org/10.1039/b003908j.